Martian Year 34 Column Dust Climatology from Mars Climate Sounder Observations: Reconstructed Maps and Model Simulations

Luca Montabone, Aymeric Spiga, David M Kass, Armin Kleinböhl, François Forget, Ehouarn Millour

Martian Year 34 Column Dust Climatology from Mars Climate Sounder Observations: Reconstructed Maps and Model Simulations

Luca Montabone[1,2], Aymeric Spiga[2,3], David M. Kass[4], Armin Kleinböhl[4], François Forget[2], and Ehouarn Millour[2]

[1]Space Science Institute, Boulder, CO, USA
[2]Laboratoire de Météorologie Dynamique (LMD/IPSL), Sorbonne Université, Centre National de la Recherche Scientifique, École Polytechnique, École Normale Supérieure
[3]Institut Universitaire de France, Paris, France
[4]Jet Propulsion Laboratory, California Institute of Technology, Pasadena, CA, USA

Key Points:

- We reconstruct sub-daily maps of column dust optical depth for Martian year 34 to be used for data analysis and modeling
- We observe seasonal, daily, and diurnal variability in the column dust, notably during the global dust event (GDE)
- Simulations with a global climate model examine the impact of the GDE on the atmospheric circulation and diurnal variability of column dust

Corresponding author: Luca Montabone, `lmontabone@spacescience.org`

Abstract

We have reconstructed longitude-latitude maps of column dust optical depth (CDOD) for Martian year (MY) 34 (May 5, 2017 - March 23, 2019) using observations by the Mars Climate Sounder (MCS) aboard NASA's Mars Reconnaissance Orbiter spacecraft. Our methodology works by gridding a combination of standard (v5.2) and novel (v5.3.2) estimates of CDOD from MCS limb observations, using an improved "Iterative Weighted Binning". In this work, we have produced four gridded CDOD maps per sol, at different Mars Universal Times. Together with the seasonal and daily variability, the use of several maps per sol also allows us to explore the diurnal variability of CDOD in the MCS dataset, which is shown to be particularly strong during the MY 34 equinoctial Global Dust Event (GDE). In order to understand whether the diurnal variability of CDOD has a physical explanation, and examine the impact of the MY 34 GDE on some aspects of the atmospheric circulation, we have carried out numerical simulations with the "Laboratoire de Météorologie Dynamique" Mars Global Climate Model. We show that the model is able to account for at least part of the observed CDOD diurnal variability. This is particularly true in the southern hemisphere where a strong diurnal wave at the time of the GDE is able to displace dust horizontally as well as vertically. The simulations also clearly show the impact of the MY 34 GDE on the mean meridional circulation and the super-rotating equatorial jet, similarly to the effects of the equinoctial GDE in MY 25.

Plain Language Summary

Large dust storms on Mars have dramatic impacts on the entire atmosphere, but may also have critical consequences for robotic and future human missions. Therefore, there is compelling need to produce an accurate reconstruction of their spatial and temporal evolution for a variety of applications, including to guide Mars climate model simulations. The recently ended Martian year 34 (May 5, 2017 – March 23, 2019) represents a very interesting case because an extreme dust event occurred near the time of the northern autumn equinox, consisting of multiple large dust storms engulfing all longitudes and most latitudes with dust for more than 150 Martian days ("sols"). We have used satellite observations from the Mars Climate Sounder instrument aboard NASA's Mars Reconnaissance Orbiter to reconstruct longitude-latitude maps of the opacity of the atmospheric column due to the presence of dust at several times in each sol of Martian year 34. These maps allow us to analyze the seasonal, day-do-day, and day-night variability of dust in the atmospheric column, which is particularly intense during the extreme dust event. We have also used simulations with a Mars climate model to show that the strong day-night variability may be partly explained by the large-scale circulation.

1 Introduction

Martian dust aerosols are radiatively active, and the dust cycle — lifting, transport, and deposition — is considered to be the key process controlling the variability of the Martian atmospheric circulations on a wide range of time scales (see e.g. the recent review by Kahre et al., 2017, and references therein). Dust storms are the most remarkable manifestations of this cycle, and one of the most crucial weather phenomena in need of study to fully understand the Martian atmosphere.

Martian dust storms are: 1. a source of strong atmospheric radiative forcing, and alteration of surface energy budget (e.g. Streeter et al., 2019); 2. a major component of the atmospheric inter-annual, seasonal, daily, and diurnal variability (see Kleinböhl et al., 2019, for an example related to the diurnal variability); 3. a way to redistribute dust on the planet via long-range particle transport (as inferred, for instance, using albedo changes: Szwast et al., 2006); 4. a means of producing perturbations of temperature and density, which propagate from the lower to the upper atmosphere, including the lower thermosphere, the ionosphere, and the magnetosphere (e.g. Girazian et al., 2019; Xiaohua et al., 2019); 5. a cause of increased loss of chemical species via escape (e.g. Fedorova et al., 2018; Heavens et al., 2018; Xiaohua et al., 2019); and 6. a source of hazards for spacecraft Entry, Descent and Landing (EDL) manoeuvres, for operations by solar-powered surface assets, and for future robotic and human exploration (e.g. Levine et al., 2018). Dust storms on Mars can be studied by using a variety of approaches: analysis of observations from satellites and landers/rovers, numerical simulations from Global Climate Models (GCM), and data assimilation techniques.

One of the most dramatic and (thus far) unpredictable events linked to Martian dust storms are the onset of a Global Dust Event — hereinafter GDE. In the literature, these events are also named "Planet-Encircling Dust Storms" (e.g. Zurek & Martin, 1993; Cantor, 2007), "Global Dust Storms" (probably the most common name), or "Great Dust Storms" (e.g. Zurek, 1982). Here we choose the denomination "Global Dust Event" because 1. even large regional storms can inject dust high enough in the atmosphere, which eventually encircles the planet, 2. these global dust events are usually characterized by several storms occurring simultaneously, or one after the other one in rapid succession, and 3. the GDE denomination was already discussed and used in Montabone & Forget (2018), and is currently adopted by several authors. However, in this paper we also argue that the key characteristics of this kind of events is their "extreme" nature, rather than their "global" nature, for which the denomination "Extreme Dust Events" would probably be even more appropriate. The Mars scientific community will need in future to define a consensus-based terminology for dust events, based on scientific arguments and measurable variables, as it is the case for other kinds of meteorological events (see, for instance, the distinction among terrestrial tropical depressions, tropical storms, and hurricanes).

In the last Martian decade (Martian Year — hereinafter MY — 25 to 34), spanning nearly two Earth decades from 2000 to 2019, three GDEs occurred: an equinoctial event in MY 25, a solstitial event in MY 28, and another equinoctial event in MY 34, starting only a few mean solar days — sols — after the corresponding onset of the MY 25 event. GDEs inject a large amount of dust particles into the Martian atmosphere, strongly modify the thermal structure and the atmospheric dynamics over several months (i.e. several tens degrees of areocentric solar longitude, L_S, see e.g. Wilson & Hamilton, 1996; Montabone et al., 2005), and impact the Martian water cycle and escape rate (Fedorova et al., 2018; Heavens et al., 2018). Similar events were previously observed in Martian Years 1, 9, 10, 12, 15, and 21 (Martin & Zurek, 1993; Cantor, 2007; Montabone & Forget, 2018; Sánchez-Lavega et al., 2019). The inter-annual variability of GDEs is irregular, and likely controlled at the first-order by the redistribution of dust on Mars over the timescale of a few years (Mulholland et al., 2013; Newman & Richardson, 2015; Vincendon et al., 2015).

The latest equinoctial GDE had its initial explosive growth in early northern fall of MY 34 (L_S approximately in the range $185°-190°$, i.e. late May 2018 – early June 2018). A regional dust storm started near the location of the Mars Exploration Rover "Opportunity". The visible opacity quickly reached a very high value of 10.8, which led to the end-of-mission of the Opportunity rover, with last communication received on June 10, 2018. The regional dust storm then moved southward along the Acidalia storm-track, and expanded both in the northern hemisphere from eastern Tharsis to Elysium (including the location of the Mars Science Laboratory "Curiosity" rover and the landing site of "InSight"), and towards the southern hemisphere (Malin et al., 2018; Kass et al., 2019; Shirley et al., 2019; Sánchez-Lavega et al., 2019; Hernández-Bernal et al., 2019).

The evolution of this MY 34 GDE in summer 2018 has been closely monitored by three of NASA's orbiters, including the Mars Reconnaissance Orbiter (MRO) and its Mars Climate Sounder (MCS) instrument (Kass et al., 2019), two of ESA's orbiters (Mars Express and the ExoMars Trace Gas Orbiter), the ISRO's Mangalyaan orbiter, and ground-based telescopes (Sánchez-Lavega et al., 2019). It has also been observed in detail from the surface by the Curiosity rover, which could still operate in dust-storm conditions thanks to its nuclear-powered system. From meteorological observations carried out aboard Curiosity with the Rover Environmental Monitoring Station (REMS), Guzewich et al. (2019) concluded that the local optical depth reached 8.5, the incident total UV solar radiation at the surface decreased by 97%, the diurnal range of air temperature decreased by 30 K, and the semidiurnal pressure tide amplitude increased to 40 Pa. Curiosity did not witness dust lifting within the Gale Crater site, which indicates that the increase in dust loading at its location is the result of dust transport from outside the crater area.

Beyond the undoubtedly interesting GDE, MY 34 also features the development of an unusually intense and large late-winter regional storm, whose peak value of column dust optical depth (CDOD) is only rivaled by the late-winter regional storm in MY 26 (reaching 75% of the peak value of the former). It is, however, reminiscent of the two global events that were successively monitored by the Viking landers in 1977 at $L_S = 205°$ and $L_S = 275°$ (Ryan & Henry, 1979; Zurek, 1982). Overall, therefore, MY 34 represents a unique year for studies linked to the onset/evolution of dust storms, and their impact on the entire Martian atmospheric system. Consequently, there is a compelling need to produce an accurate reconstruction of the spatial and temporal evolution of the dust optical depth in MY 34, particularly covering the GDE, but also putting the unprecedented weather measurements acquired by the InSight lander during the late-winter regional storm into global context (Spiga et al., 2018).

Montabone et al. (2015) developed a methodology to grid values of CDOD retrieved from multiple polar orbiting satellite observations, such as NASA's Mars Global Surveyor (MGS), Mars Odyssey (ODY), and MRO. Using this methodology (a combination of "Iterative Weighted Binning" — IWB — and kriging spatial interpolation), they were able to produce multi-annual datasets of daily CDOD maps extending from MY 24 to MY 33, which are publicly available on the Mars Climate Database (MCD) project webpage at `http://www-mars.lmd.jussieu.fr/` (look for "Martian dust climatology" on the MCD webpage). The datasets include both irregularly gridded maps (because of the presence of missing grid point values after the application of the IWB, where observations are not available) and regularly kriged ones. The kriged maps can be used as a daily, column-integrated "dust scenario" to prescribe or guide the evolving atmospheric dust distribution in numerical model simulations.

In this paper we describe how we make use of newly processed dust opacity retrievals from thermal infrared observations of the MRO/MCS instrument (McCleese et al., 2007) in order to reconstruct maps of column dust optical depth specifically for MY 34, and describe aspects of the two-dimensional dust climatology. In Section 2, we discuss the improvements both to the MCS retrievals and to the gridding methodology described in Montabone et al. (2015). In Section 3, we analyze in general terms the CDOD variability at seasonal timescale, and in specific terms the daily evolution of the GDE and late-winter dust storm. We also address the diurnal variability observed when reconstructing multiple CDOD maps per sol. In Section 4, we use simulations with the Laboratoire de Météorologie Dynamique Mars GCM (LMD-MGCM) in order to 1. assess some of the impacts of the MY 34 GDE on the Martian atmospheric circulation (in this case the model dust distribution is guided by the kriged maps), and 2. verify that the GCM is able to reproduce at least part of the diurnal variability observed in the reconstructed multiple CDOD maps per sol (in this case the model dust distribution is only initiated using the kriged maps, but is not subsequently guided). Conclusions are drawn in Section 5.

2 Building column dust optical depth maps

The methodology described in Montabone et al. (2015) to grid CDOD values using the IWB, and to spatially interpolate the daily maps using kriging, has been applied to observations by MGS/Thermal Emission Spectrometer (TES), ODY/Thermal Emission Imaging System (THEMIS), and MRO/MCS from MY 24 to MY 32. For MY 33, because of the progressive change in local time of THEMIS observations, we have introduced a weighting function specific for the THEMIS dataset in order to favor the MCS dataset (i.e. we simply apply a 0.5 weight to THEMIS CDODs during the first iteration with the time window of 1 sol, reduced to 0.1 for the subsequent iterations using larger time windows. The impact of THEMIS observations is therefore reduced to 50% or 10% with respect to MCS ones). As mentioned in the introduction, version 2.0 (v2.1 for MY 33) of both irregularly gridded maps and regularly kriged ones (we refer to the latter as the column-integrated "dust scenario" in this paper) are available on the MCD project website.

For the specific case of the MY 34 GDE, the MCS team has updated their retrievals of temperature, dust and water ice profiles. We have correspondingly updated the gridding/kriging methodology with the aim of producing a more refined and accurate climatology, both for scientific studies and for the use in numerical model simulations. Therefore, in the following we describe how we reconstruct CDOD maps for MY 34 (currently version 2.5). We provide some details about the differences between current and previous versions (i.e. v2.2, v2.3, and v2.4) in Appendix A.

2.1 Observational dataset

In MY 34, single THEMIS CDOD retrievals are no longer available. Because of the late local time of THEMIS observations in MY 34, Smith (2019) had to develop a "stacking" algorithm that assesses how a group of THEMIS spectra in a L_S/latitude bin change as a function of estimated thermal contrast. Therefore, we do not use THEMIS any more in MY 34, and we completely rely on estimated CDODs from MCS.

Dust opacity retrievals from thermal infrared observations of the MCS instrument aboard MRO are described in Kleinböhl et al. (2009); Kleinböhl et al. (2011), and Kleinböhl et al. (2017a). The currently standard MCS dataset, based on the v5.2 "two-dimensional" retrieval algorithm specifically described in (Kleinböhl et al., 2017a), has been reprocessed by the MCS team for the time of the MY 34 GDE to obtain better coverage in the vertical and, therefore, more reliable estimates of CDOD values during the event (Kleinböhl et al., 2019). This latest MCS dataset, only available between May 21, 2018 ($L_S \approx 179°$) and October 15, 2018 ($L_S \approx 269°$), and labelled v5.3.2, is an interim version that includes the use of a far infrared channel for retrievals of dust. The differences between MCS retrievals version 5.2 and 5.3 are as follows:

- Use of B1 detectors to extend the dust profile retrieval: the dust extinction efficiency in channel B1 at 32 μm is only about half the value of channel A5 at 22 μm (Kleinböhl et al., 2017b), which is the primary channel for dust retrievals, allowing profiles to extend deeper by 1 to 1.5 scale heights;
- Accepting a higher aerosol to CO_2 gas opacity ratio along the line-of-sight in the temperature retrieval channel A3;
- Modifications for determining surface temperature when there are no matching on-planet views (primarily cross-track views) to improve the performance under high dust conditions when the array is lifted and limb views do not intersect the surface.

CDODs are estimated by integrating the dust opacity profiles after an extrapolation from the lowest altitude at which profile information is available, under the assumption of homogeneously mixed dust (see Fig. 1 of Kleinböhl et al., 2019, as well as Fig. 15 in this paper). For the reconstructed CDOD maps in MY 34, we use MCS v5.3.2 estimated CDODs from $L_S \approx 179°$ to $L_S \approx 269°$, and MCS v5.2 otherwise.

2.2 Data Quality Control

A general discussion about the limitations of using CDOD estimates from MCS is included in Montabone et al. (2015), specifically Section 2.1.2. As mentioned in the previous sub-section, the extended vertical coverage in MCS v5.3.2 helps estimate CDODs more accurately. In the present work, therefore, we have improved the definition of the Quality Control (QC) procedure with respect to the one used in Montabone et al. (2015), particularly by allowing a more extensive use of dayside observations. We define dayside observations as those with local times (lt) in the range 09:00 $<$ lt $\leq$ 21:00, although most of dayside observations at low latitudes have local times close to 15:00. Nightside observations are defined as those outside the dayside range, with most nightside observations at low latitude having local times close to 03:00.

We need to stress that, despite the improvements in MCS v5.3.2, the main issue for estimating column optical depths using limb observations remains the fact that many opacity profiles have rather high cut-off altitudes (particularly dayside ones, see also right column of Fig.5), due to either dust or water ice opacities that are too large. During the dust storms, cutting off due to dust, and extrapolating over a big altitude range under the assumption of homogeneously mixed dust, provide reasonable CDODs, although increase the uncertainty on the column values. However, when the profile is cut-off due to water ice, the dust column is poorly constrained due to the extrapolation. Because water ice clouds are a dominant source of questionable CDOD values, especially on the dayside, we specifically apply stringent filters when we suspect the dust opacity is likely contaminated by the water ice opacity. Conversely, we relax our filtering for dayside values during the dust storms, when water ice clouds are not likely to be present.

Note that MCS is also able to observe cross-track, thus providing information within a range of local times at selected positions during the MRO orbits (Kleinböhl et al., 2013). We have also better defined a dust quality flag in MCS v5.3.2 to help filter those observations where a significant number of detectors were excluded in the retrieval of the dust opacity profile, because of radiance residuals exceeding threshold values (Kleinböhl et al., 2009). Each excluded detector corresponds to a truncation of about 5 km in the reported profile compared to the altitude range that was originally selected by the retrieval algorithm based on line-of-sight opacity.

We apply the following QC procedure to the MCS CDOD values at 21.6 μm in extinction:

- To discard values when they are most likely contaminated by CO_2 ice (i.e. if, at any level below 40 km altitude, the temperature is $T < T_{CO_2} + 10$K, and the presumed dust opacity is larger than 10^{-5} km^{-1});
- To discard values when water ice opacity is greater than dust opacity at the cut-off altitude of the corresponding dust profile;
- To discard cross-track CDODs with cut-off altitudes higher than 8 km (i.e. the corresponding dust opacity profiles do not extend down to 8 km altitude or lower), because they are likely to produce questionable CDODs;
- Dayside values are specifically filtered based on a cut-off altitude that depends on the MCS retrieval version and the amount of ice that is present. The threshold cut-off altitude is 8 km during the icy MCS v5.2 prior to $L_S = 179°$. It increases to 16 km during the icy MCS v5.3.2 data period prior to the start of the GDE ($179° < L_S < 186.5°$). There is no threshold cut-off altitude during the GDE with v5.3.2 available ($186.5° \leq L_S \leq 269°$). The threshold cut-off altitude was reinserted at 8 km after the GDE with icy conditions and MCS v5.2 data in the period $269° < L_S \leq 312°$. During the late winter regional dust storm under less icy conditions, the MCS v5.2 data threshold cutoff altitude was again increased to 16 km ($312° <$

$L_S < 350°$) to return to 8 km after the end of the storm and following possible presence of the ice clouds ($L_S \geq 350°$);

- To discard CDODs when more than 1 detector is excluded inside the limits of the MCS v5.3.2 ($179° \leq L_S \leq 269°$) as well as if any detector is excluded in MCS v5.2 during the late-winter dust storm ($312° < L_S < 350°$);
- To assign a fixed value of 0.01 to very low values of CDOD < 0.01 having cut-off altitude higher than 4 km.

We plot in Fig.1 the percentage number of CDOD values that are flagged by each individual filter, together with the total of the filtered values after the application of the complete QC procedure. The total does not correspond to the sum of each single filter, as a CDOD value can be flagged by multiple filters. This figure clearly shows that the presence of water ice in spring and summer strongly affects the number of CDOD values passing the QC. Dayside values are also problematic because their corresponding dust profiles usually have rather high cut-off altitudes, compared to nightside values. Cross-track values have the tendency to exhibit rather high cut-off altitudes as well, and lead to questionable column dust optical depths. As a consequence, a large number of them at low- and mid-latitudes are discarded throughout the year. Observations where more than one detector was excluded in the retrieval are about 20% throughout MCS v5.3.2. The number of values filtered because of possible carbon dioxide ice contamination is relatively low throughout the year (less than 10%).

After QC, the number of available values is plotted in Fig.2, separated into nightside and dayside values. The aphelion cloud belt and the winter polar hoods are mainly responsible for the lack of data at equatorial latitudes in the dayside plot, and at high latitudes in both dayside and nightside plots. The implementation of the new "water ice" filter is effective in reducing the probability that the lowest levels of the dust profiles are contaminated by the presence of clouds, but there is a risk of filtering out retrievals that actually may have been usable, particularly at high latitudes. A refinement of this filter should be addressed in future work. Vertical bands with no data are periods when MCS did not observe.

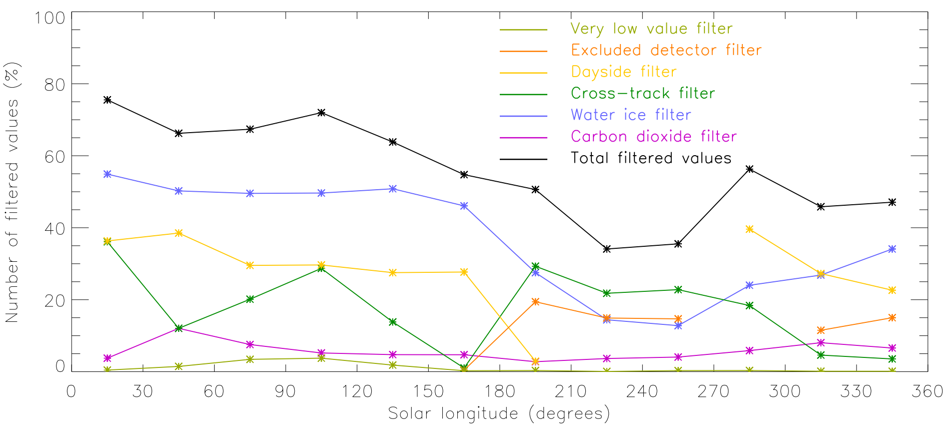

Figure 1. Percentage number of CDOD values flagged by each individual filter in the QC procedure within 30° L_S ranges in MY 34 (color lines), together with the percentage total number of filtered CDODs after the application of the complete QC procedure (black line). The numbers are associated to the middle of each 30° L_S range. Note that the "excluded detector" filter does not apply before $L_S = 179°$ and for $269° < L_S < 312°$, and that the "dayside" filter does not apply during the GDE ($186.5° \leq L_S \leq 269°$).

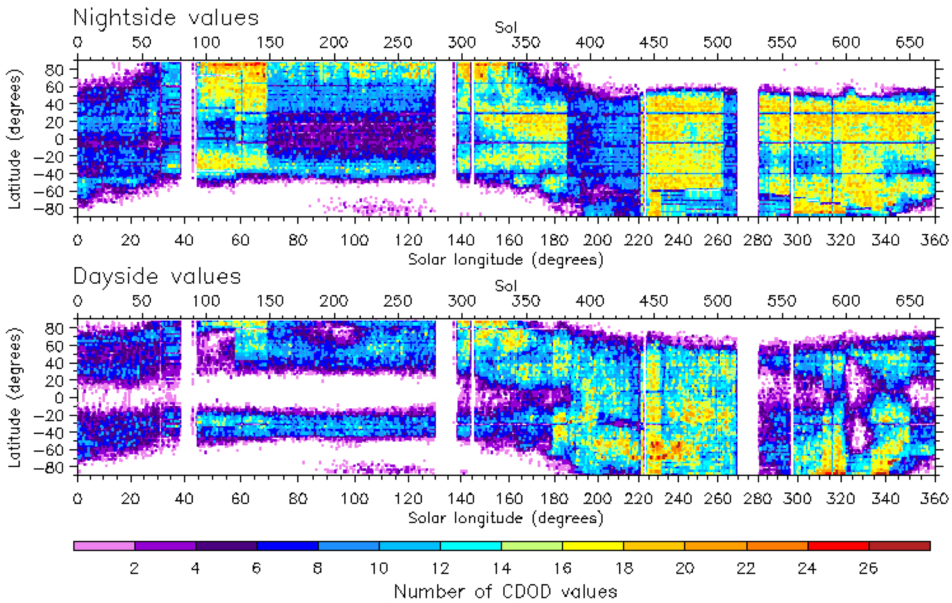

Figure 2. Number of nightside (upper panel) and dayside (lower panel) values of column dust optical depth available for gridding after passing the quality control procedure described in the text. The number of values is summed in 1 sol × 2° latitude bins, and plotted as a function of time and latitude, where time is shown both as sol from the beginning of MY 34 and as areocentric solar longitude. Dayside observations are defined to have local times between 09:00 (excluded) and 21:00 (included), whereas nightside observations are defined to have local times between 00:00 and 09:00 (included) as well as between 21:00 (excluded) and 24:00.

2.3 Data uncertainties and processing

Together with the QC procedure, we have also revised the empirical method to estimate the uncertainties on the MCS CDOD values at 21.6 μm in extinction, with respect to the one used in Montabone et al. (2015). We apply the following relative uncertainties:

- 10% for CDOD values < 0.01 having cut-off altitude higher than 4 km (i.e. for those values replaced with CDOD=0.01);
- 5% for CDOD values < 0.01 or values with cut-off altitudes lower than 4 km;
- When CDOD ≥ 0.01 or cut-off altitude ≥ 4 km, we assign the largest relative uncertainty between the one calculated as a linear function of CDOD ($\frac{15}{1.49}\cdot$CDOD$+\frac{7.3}{1.49}$) and the one calculated as a linear function of the cut-off altitude ($\frac{25}{21}\cdot$alt$+\frac{5}{21}$). The two functions are defined in such a way that, for instance, the uncertainty is 5% if CDOD = 0.01 or cut-off altitude = 4 km, 20% if CDOD = 1.5, and 30% if cut-off altitude = 25 km.

As detailed in Montabone et al. (2015), further data processing consists in converting MCS CDODs from 21.6 μm in extinction to absorption-only 9.3 μm by multiplying by 2.7, to be consistent with the climatologies of the previous Martian years. We then normalize the values to the reference pressure level of 610 Pa, but instead of using the surface pressure value calculated by the MCD `pres0` routine (Forget et al., 2007), we now use the same surface pressure value used for the corresponding MCS retrieval. MCS retrieves pressure at the pointing altitude where it is most sensitive to pressure (typically

20-30 km, see Kleinböhl et al., 2019), from which surface pressure can be extrapolated with an uncertainty estimate based on pointing uncertainty. In conditions where a pressure retrieval is unsuccessful (typically in conditions of high aerosol loading), the MCS algorithm uses pressure derived from the climatological Viking surface pressure (Withers, 2012). In this case, the uncertainty of the surface pressure is derived from the daily root mean squared of surface pressure from the MCD v5.3, interpolated at the specific location and season of an observation using a pre-built 5° L_S × 5° latitude array (as described in Section 2.3 of Montabone et al., 2015).

2.4 Gridding methodology

In this work we closely follow the basic principles of reconstructing CDOD maps, which are detailed in Section 3 of Montabone et al. (2015). Iterative Weighted Binning (IWB) is applied to CDOD values and uncertainties at 9.3 μm in absorption, normalized to 610 Pa, to produce gridded values on a 6° longitude × 5° latitude map. The current criterion to accept a value of weighted average at a particular grid point at any given iteration is that there must be at least one observation within a distance of 200 km from the grid point, otherwise a missing value ("Not-a-Number", or NaN) is assigned to that grid point. The other used parameters as listed in Table 1 of Montabone et al. (2015) for MCS remain the same.

The application of the IWB for a sol in the growth phase of the GDE when the Mars Universal Time (i.e. the local time at 0° longitude) is MUT = 12:00 (noon) is shown in Fig. 3. In the left column we plot the CDOD observations effectively used for gridding, while in the right column we plot the result of the gridding. The time window (TW) for considering single observations increases from 1 to 7 sols going from the upper to the lower row. All four iterations are applied when reconstructing a map, and each iteration with larger TW only fills NaN grid points left by the previous iterations with smaller TWs. By doing this, each map is always built around the most up-to-date observations, usually provided by the iteration with TW = 1 sol (unless there are missing observations for one or more sols). In general, the value of each valid grid point of a map is assigned using observations within the smallest possible time window. For this reason, daily maps respond to rapidly changing events, such as the onset of a dust storm, as quickly as single observations allow. Obviously, for a polar, Sun-synchronous satellite such as MRO there is an intrinsic limitation to the production of a synoptic map, given by the fixed local times of observations.

The key differences we have introduced in this work with respect to the methodology described in Section 3 of Montabone et al. (2015) are that we now opportunely separate the contribution of dayside and nightside observations, and we create four gridded maps per sol at four different MUTs. We achieve this by 1. only considering observations with local times within ±7 hours of the local time of a given grid point, in each TW iteration, and 2. repeating the IWB procedure for observations centered at MUT = 00:00, 06:00, 12:00, and 18:00, rather than simply at MUT = 12:00 (this is equivalent to a 6-hour rather than a 24-hour moving average).

The effect of applying a ±7 h window selection for observations to be gridded at each grid point can be already appreciated in Fig. 3, where the distinction between nightside tracks (positive slope) and dayside ones (negative slope) is evident, at each TW iteration. Because we use a local time window of ±7 h, there is a superposition of nightside and dayside values at some longitudes, which allows for a smoother transition between the two. In Fig. 4 we show an example of the combined effect of the updated methodology for the same sol of Fig. 3, but only for the last iteration with TW = 7 sol (we stress that all four iterations with increasing TWs are always applied at each MUT, though). In the left column we plot the CDOD observations effectively used for gridding in the four maps of the right column, with MUT = 00:00, 06:00, 12:00, and 18:00.

The difference in local time between each observation and the map grid point close to which it is located is plotted in the left column of Fig. 5, using the same observations of the left column of Fig. 4. Since in Fig. 5 we only show examples with TW = 7, there are multiple orbit tracks with similar local time differences, but belonging to different sols. For each map with different MUT, there are two longitude ranges (with local times around 03:00 and 15:00) within which these differences are small, although only one orbit track also matches the specific sol. The most current update of CDOD in each map is therefore confined to these two longitude ranges. The weights on time, distance, and quality of observation (see details in Section 3.2 of Montabone et al., 2015) eventually define the contribution of each single observation to the grid point average (plotted in the right column of Fig. 4 only for the last iteration).

It is necessary to discuss the differences among the maps at different MUTs, because these are the novel result of this work. When looking at the four MUT maps in the right column of Fig. 4, in fact, a clear diurnal variation of CDOD can be appreciated, particularly pronounced in the latitude band 20°S−70°S (see also Section 3 and Fig. 14). This variation of CDOD has the characteristics of a Sun-synchronous wave with wavenumber one: smaller optical depths are found at night, larger optical depths occur during the day. The diurnal variation is already present in the estimated MCS CDODs, as shown in the left column of Fig. 4, and is not an artefact of the gridding methodology, nor is it limited to the sol showed in Fig. 4, as Fig. 14 clearly demonstrates. Furthermore, this strong diurnal variation of CDOD corresponds very well both in L_S (during the growth phase of the GDE) and in latitude to the strong diurnal variation of the MCS dust opacity profiles, as described in Kleinböhl et al. (2019). In that paper, GCM simulations are used to reproduce the diurnal variability of the dust profiles, and help explain the likely dynamical effects at the origin of this phenomenon.

The question arises, then, whether the diurnal variability observed in estimated MCS CDOD can also have a dynamical origin, or can be explained otherwise. We address the possibility of a dynamical origin with GCM simulations in Section 4, while we point out here that interpreting results from MCS CDODs is particularly challenging, as already mentioned in Subsection 2.2. The right column of Fig. 5, in fact, shows that the dust opacity profiles (from which CDODs are estimated) in the latitude band where the diurnal CDOD differences are more pronounced have quite different cut-off altitudes above the local surface between day and night: nightside profiles tend to extend lower in altitude, while dayside profiles are generally cut at higher altitudes. This is due to several factors, although it is primarily driven by the altitude at which the retrieval algorithm finds the atmosphere too opaque in the limb path. The increase in the amount of dust or water ice (and their vertical extent) in the dayside profiles causes the profiles to terminate further from the surface than the nightside ones, on average. As previously pointed out, the different cut-off altitudes for nightside and dayside retrievals imply that the uncertainty in the CDOD extrapolation is larger during the day, but it does not necessarily imply that the homogeneously mixed dust assumption is not valid, particularly during the peak of the GDE. We refer to Section 3 for in-depth discussion on this topic.

2.5 Reference MY 34 dust climatology

The gridded and corresponding kriged maps of CDOD described in Montabone et al. (2015) have been used as reference multi-annual dust climatology in several studies and applications, including the production of MCD statistics. It is, therefore, compelling to produce a reference MY 34 climatology following the approach established for the previous Martian years.

Although in this work we produce four gridded maps per sol, we calculate the diurnal average and we use only one map per sol to build the reference MY 34 climatology. We do so because 1. the diurnal variability of MCS CDOD is not yet soundly con-

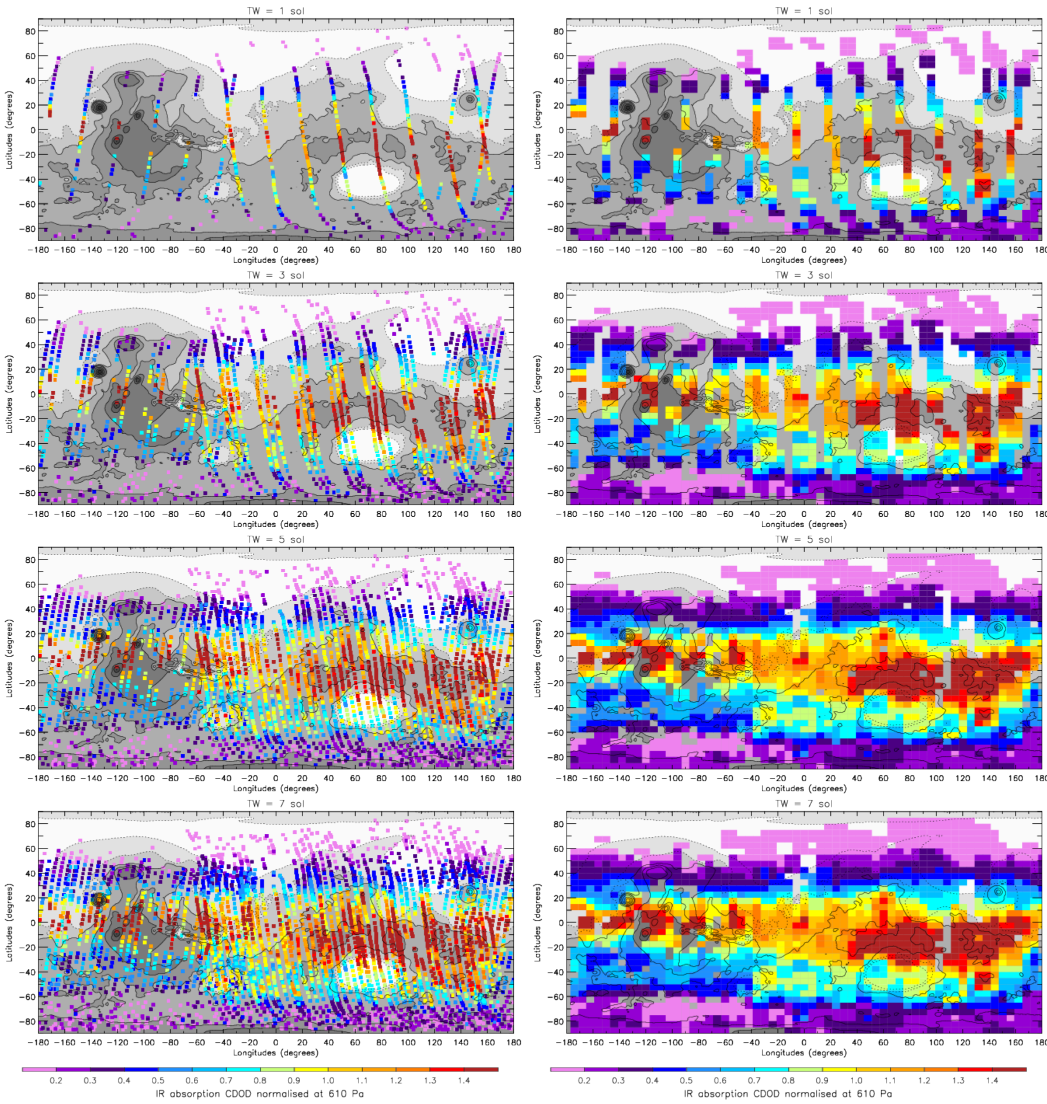

Figure 3. This figure shows longitude-latitude gridded maps (right column) built using CDOD observations (left column) selected within four iterative time windows (TW = 1, 3, 5, and 7 sols, from top to bottom). All maps have MUT = 12:00, and are representative of the sol-of-year (SOY) 400, $L_S \approx 196°$, in the growth phase of the GDE (The SOY is the integer sol number starting from SOY=1 as first sol of the year). The CDODs are IR absorption (9.3 μm) values normalized to 610 Pa. The rows from top to bottom illustrate the application of the IWB procedure (including the use of the four subsequent time windows) at a fixed MUT. The final result of the iteration is the map in the bottom right position.

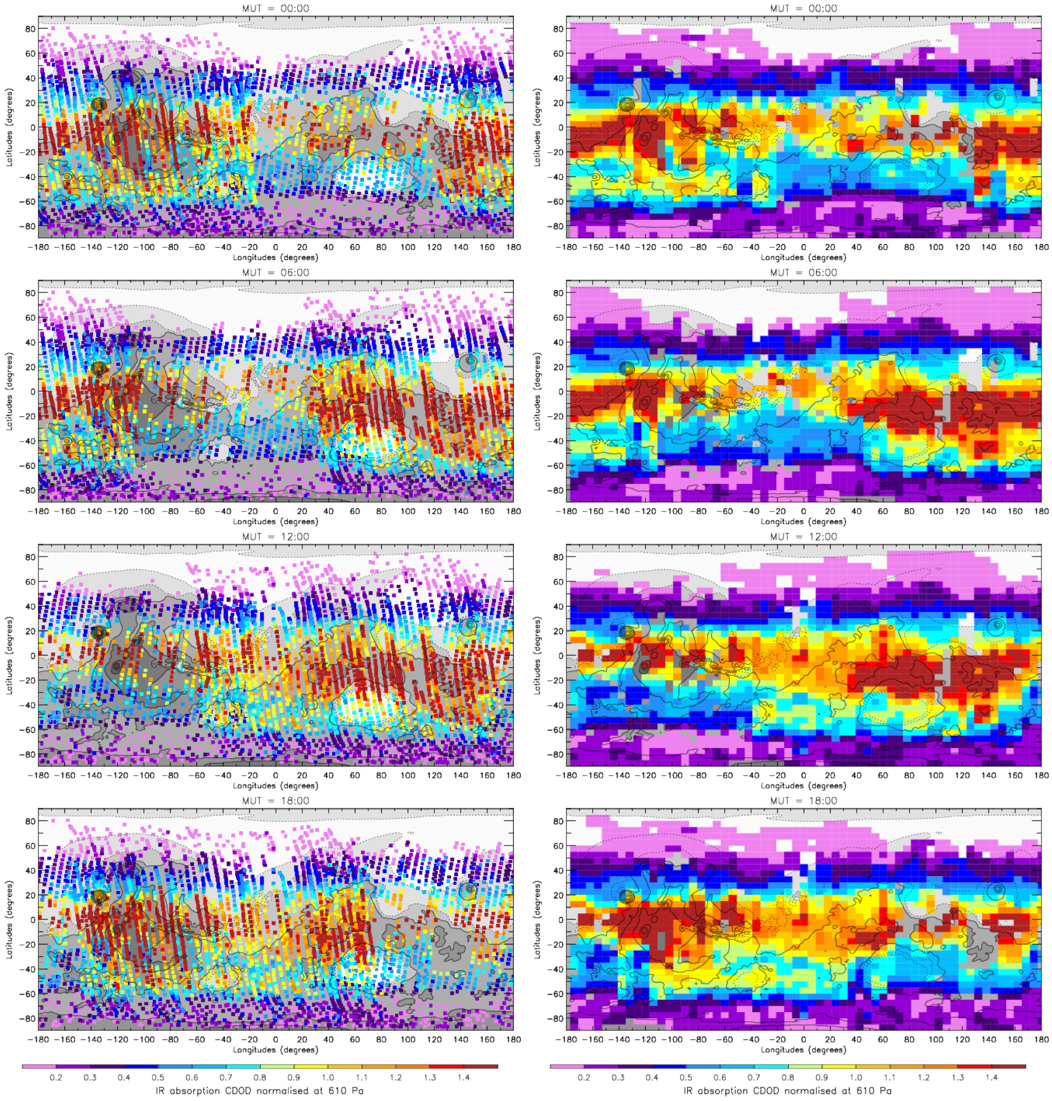

Figure 4. This Figure shows longitude-latitude gridded maps (right column) built using CDOD observations (left column) selected within a time window of 7 sols (after the iterative application of time windows of 1, 3, and 5 sols, as in Fig. 3) at four different Mars Universal Times: MUT = 00:00, 06:00, 12:00, and 18:00, from top to bottom. These maps are representative of the four different MUTs in sol-of-year (SOY) 400, $L_S \approx 196°$, in the growth phase of the GDE (This is the same SOY shown in Fig. 3 only for MUT = 12:00). The CDODs are IR absorption (9.3 µm) values normalized to 610 Pa. Each row of this figure illustrates how the last iteration of the IWB procedure is applied to eventually produce one map every 6 hours.

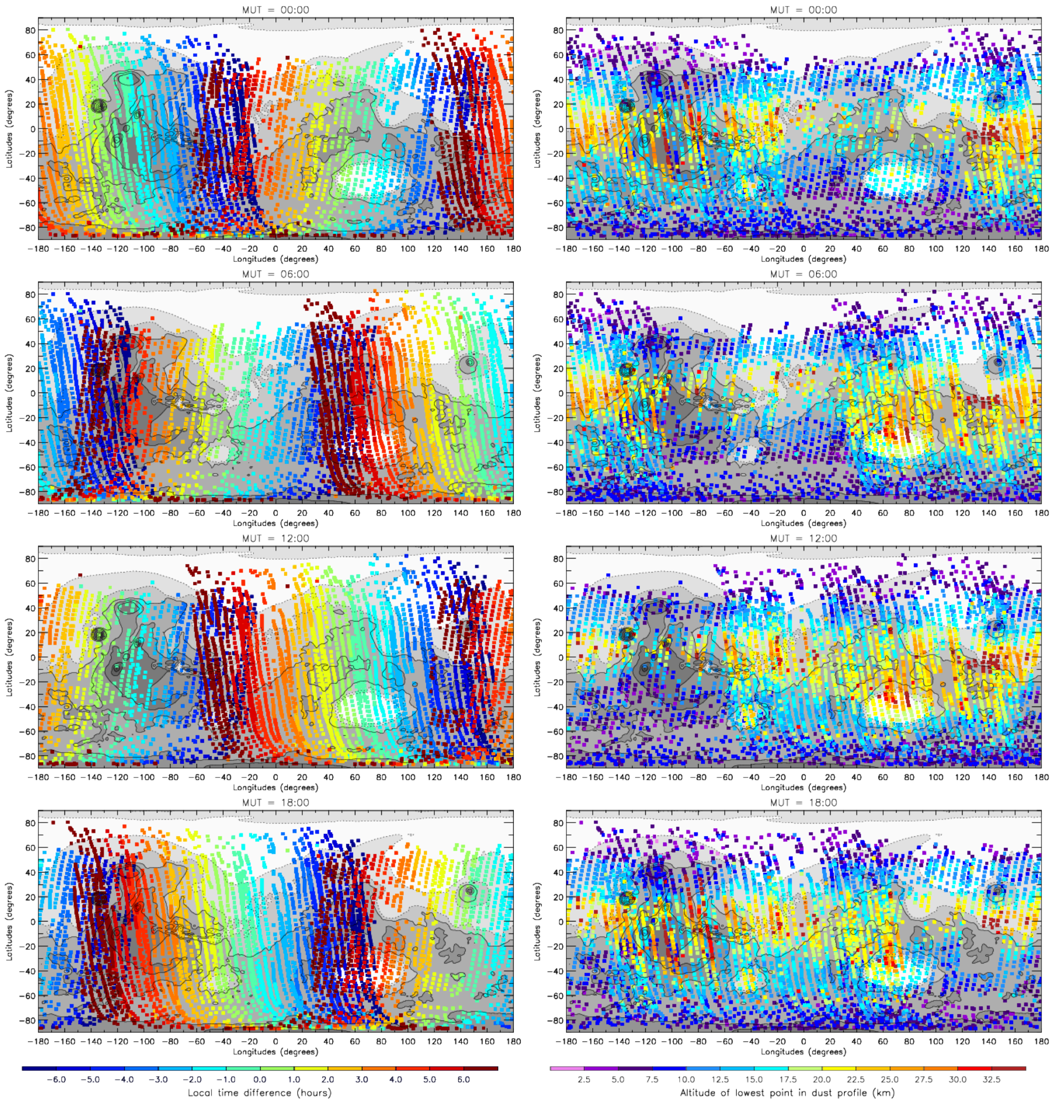

Figure 5. In this Figure we plot the same observations shown in the left column of Fig. 4 for MUT = 00:00, 06:00, 12:00, and 18:00, color coded according to: (left column) the difference in local time between each observation and the map grid point around which it is located, and (right column) the cut-off altitude above the local surface of the dust opacity profile corresponding to each estimated CDOD observation.

firmed by independent observations, 2. it is not clear whether using a column-integrated dust scenario with diurnal variability in model simulations would not trigger spurious effects, e.g. erroneously forcing the tides, and 3. we would like to be consistent with climatologies from previous Martian years. There is also a technical issue complicating the production of diurnally-varying kriged maps, which is the fact that some of the sub-daily gridded maps have many missing values, particularly when the water ice opacity affects the dust opacity.

We show in Fig. 6 an example of the diurnally-averaged gridded map and corresponding kriged one, for the same sol as in Fig. 3. The diurnally-averaged maps are more complete than any single MUT map, and rather spatially smooth. The transition to maps at previous and subsequent sols is also rather smooth (see e.g. Figs. 11 and 13). We should mention that, in contrast to Montabone et al. (2015), we no longer modify the values of the gridded maps in a latitude band around the southern polar cap edge before applying the kriging interpolation. This was previously done to artificially introduce climatological "south cap edge storms" and balance TES and MCS years in term of dust lifted at the south cap edge. The use of MCS v5.3.2 retrievals extending to lower altitudes, and the fact that TES CDOD retrievals at the south cap edge are being revised (M. Smith, personal communication) alleviate the need for such correction.

The MY 34 daily maps of gridded and kriged IR absorption CDOD normalized to 610 Pa are included in NetCDF files together with maps of several other variables, as mentioned in Appendix B of Montabone et al. (2015). We note here that the number of observations, the time window, and the reliability value for valid grid points are calculated as diurnal averages. The uncertainty is calculated as combined uncertainty of the four sub-daily values with equal weights. The combined RMSD is calculated as the square root of the average of the squared RMSDs of the four sub-daily values (also with equal weights). We separately provide the RMSD of the diurnally averaged values, which is an indicator of the diurnal variability. We also note that, following the Montabone et al. (2015) sol-based Martian calendar (see their Appendix A for a description), MY 34 has 668 sols, therefore we provide 668 gridded maps — MY 34 new year's L_S is 359.98°. The column-integrated dust scenario, though, has always 669 kriged maps for practical reasons, hence the last sol of the MY 34 dust scenario is the first sol of MY 35. Both gridded and kriged maps version 2.5 for MY 34 are publicly available at the dedicated "Martian dust climatology" webpage on the MCD project website hosted by the LMD at the URL: `http://www-mars.lmd.jussieu.fr/`. They are also available on the "Institut Pierre-Simon Laplace" (IPSL) data repository at the URL: `https://data.ipsl.fr/catalog/`. For completeness, we have also made the diurnally-varying gridded maps (identified as version 2.5.1) available on both sites. See the "Data availability" section at the end of this paper for detailed access information.

2.6 Validation

An important aspect of producing a reference dataset for the dust climatology is its validation with independent observations. The Opportunity rover entered safe mode right at the onset of the GDE, while the Curiosity rover took measurements of visible dust optical depth throughout the GDE using its MastCAM camera (Guzewich et al., 2019). Hence, we use measurements from Curiosity for validation, together with publicly available visible images taken by the Mars Color Imager (MARCI) camera aboard MRO.

Figure 7 show the comparison between the time series of the dust optical depth (sol-averaged and normalized to 610 Pa) observed by Curiosity in Gale crater during the GDE (Guzewich et al., 2019), and the time series of CDOD extracted from the gridded maps and averaged in a longitude-latitude box centered on Gale crater (after conversion to equivalent visible values). The gridded maps are able to fairly well reproduce the timing and

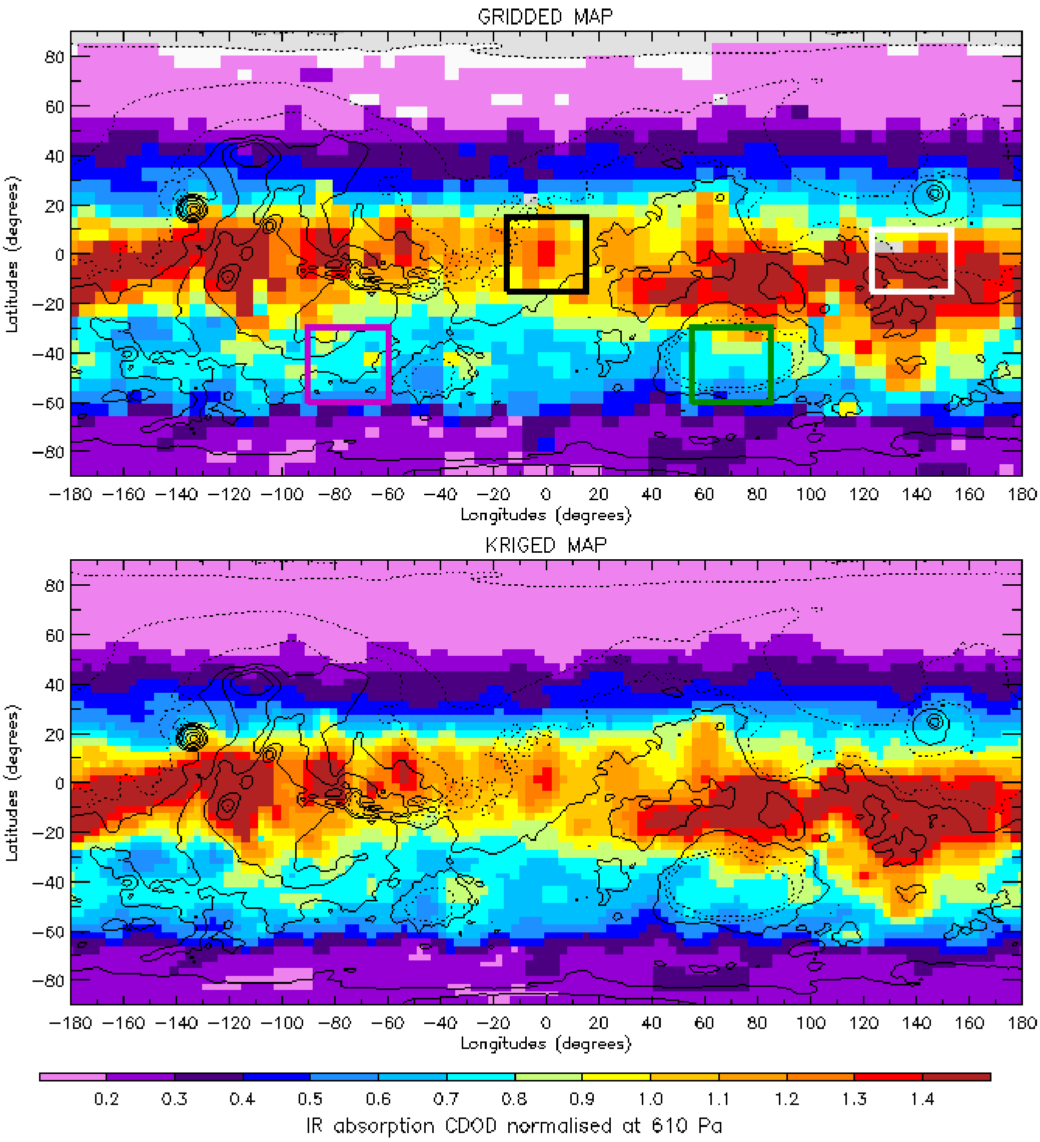

Figure 6. Diurnally-averaged gridded map (upper panel) and corresponding kriged map (lower panel) of 9.3 μm absorption column dust optical depth for SOY 400, $L_S \approx 196°$, in the growth phase of the GDE. The gridded map showed here is the diurnal average of the four maps in the right column of Fig. 4. The spatial resolution of the gridded map is 6° longitude × 5° latitude, whereas the resolution of the kriged one is 3° longitude × 3° latitude. The white rectangle in the gridded map highlights the averaging area around Gale crater used in Fig. 7 for comparison with the CDOD measured by the Curiosity rover. The other colored squares highlight the averaging areas in Aonia Terra (magenta), Meridiani Planum (black) and Hellas Planitia (green) used in Fig. 14

decay of the GDE around Gale, but they underestimate the peak of the event. Furthermore, they overestimate the decay between $L_S \approx 205°$ and $L_S \approx 215°$, although within the uncertainty limit. Spatial inhomogeneity in the CDOD field, even during the mature phase of the GDE, may account for some of the differences. Looking within the white box over Gale Crater in the gridded map of Fig. 6 (which is at $L_S \approx 196°$, i.e. at the opacity peak for Curiosity), the northern third of the box has substantially lower opacity values. Regional (especially latitudinal) gradients can, therefore, be one of the causes of the peak difference. Also note that Gale crater is a challenging location for MCS to observe due to MRO providing relay services to the Curiosity rover. In particular the number of in-track profiles is limited and may be geographically biased. See also further comments about the comparison with Curiosity data in Section 4 when discussing Fig. 16. Finally, we note that the time series using the kriged maps is nearly identical to that using the gridded ones (i.e. the magenta line in Fig. 7), although we do not show this here.

We show the comparison between one of our gridded CDOD maps and a MARCI image in Fig. 8. The comparison is done for June 6, 2018, at the onset of the GDE, which corresponds to SOY 387 in our dataset. The extension of the dust cloud in both the MARCI image and the CDOD map is similar, with both showing intense activity around Meridiani, an eastward progression of the storm, and relatively clear skies over the Tharsis volcanoes. This specific CDOD map fails to show the onset of the south polar cap edge dust activity, but maps at subsequent sols do.

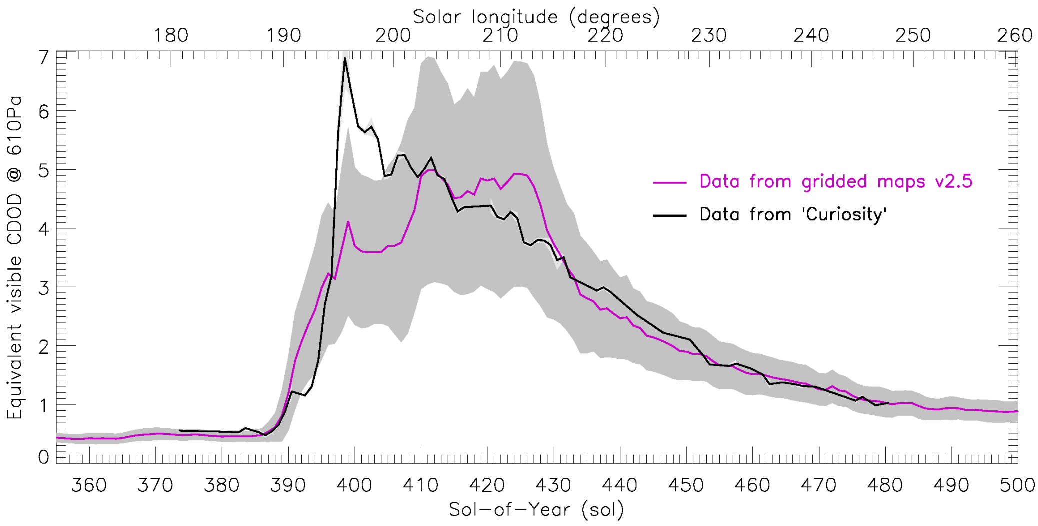

Figure 7. Time series of equivalent visible column dust optical depth calculated from the 9.3 μm absorption CDOD normalized to 610 Pa, extracted from the diurnally-averaged gridded maps in an area around Gale crater (magenta line), compared to the time series of visible column optical depth measured by MastCAM aboard NASA's "Curiosity" rover (black line). Curiosity observations (Guzewich et al., 2019) have been diurnally-averaged and normalized to 610 Pa (using the surface pressure from the Mars Climate Database `pres0` routine). Both time series are shown between Sol-of-Year 355 and 500, i.e. $L_S \approx 170° - 260°$. We used a factor of 2.6 to convert 9.3 μm absorption CDODs into equivalent visible ones. Data from gridded maps are averaged in the area shown by a white rectangle in Fig. 6 (i.e. longitudes 123°E − 153°E, latitudes 15°S − 10°N) centered around Curiosity landing site at longitude 137.4°E and latitude 4.6°S. Light and dark grey shades show the uncertainty envelope (1-sigma) respectively for Curiosity's time series and the time series extracted from the gridded maps.

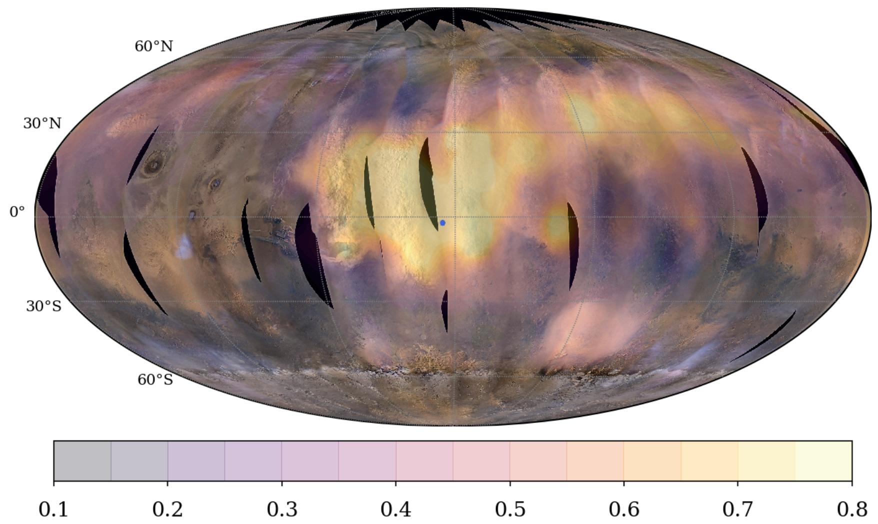

Figure 8. The background global image of Mars in this Figure is referenced PIA22329 in the NASA photojournal (credits: NASA/JPL-Caltech/MSSS). We wrapped this map on a Mollweide projection. It shows the growing MY 34 GDE as of June 6, 2018. The map was produced by the Mars Color Imager (MARCI) camera on NASA's Mars Reconnaissance Orbiter spacecraft. The blue dot shows the approximate location of the Opportunity rover. We overlay on this image the column dust optical depth kriged map for the corresponding sol (sol-of-year 387), which we have reconstructed from MCS observations. The IR absorption (9.3 μm) CDOD map (not normalized to 610 Pa) is plotted as filled colored contours.

3 Seasonal, daily, and diurnal variability of column dust

In this Section we analyze the variability at different temporal scales, which is included in the MY 34 dust climatology reconstructed from MCS CDODs. In particular, we look at the seasonal, daily, and diurnal variability, as shown in Figures 9 to 15.

Starting from the seasonal variability, Fig. 9 shows the latitude vs time plot of the zonally and diurnally averaged CDOD obtained from both the gridded maps and the kriged ones. This comparison shows that the kriged maps have the advantage of being complete (i.e. CDOD values are assigned at every grid point) while preserving the overall properties of the dust distribution. Montabone & Forget (2018) noted that Martian years show two distinctive seasons with respect to the atmospheric dust loading, when a comparison of multi-annual zonal means of CDOD is carried out: a "low dust loading" (LDL) season between $L_S \approx 10°$ and $L_S \approx 140°$, and a "high dust loading" (HDL) season at other times, when regional dust storms and global dust events are most likely to occur — commonly referred to as the "dust storm season". MY 34 does not differ, as dust started to increase above the 0.15 level (IR absorption at 9.3 μm) after $L_S \approx 160°$, following a quiet LDL season (see Fig. 10 as well, which is the time series obtained from the latitude vs time plot by averaging also in the latitude band 60°S − 40°N).

Nevertheless, the optical depth abruptly increased after $L_S \approx 186°$ due to the onset of the GDE, which rapidly grew to the west of Meridiani Planum, expanded eastwards and southwards, and spread a large amount of dust at all longitudes within approximately a latitude band 60°S−40°N (see its daily evolution over 12 sols in Fig. 11), then slowly decayed over about 130 sols, as can be observed from the tail of the GDE peak in Fig. 10.

MY 34 also featured two other maxima in CDOD that are climatologically consistent with all other 10 previously observed years: one at southern polar latitudes centered at $L_S \approx 270°$, and the other in the latitude band 60°S − 40°N peaking at $L_S \approx 325°$. These maxima are linked respectively to a regional dust storm occurring over the ice-freed southern polar region, and to a particularly intense late-winter regional storm (see its daily evolution over 12 sols in Fig.13). The latter has the characteristics of a flushing storm following the Acidalia-Chryse storm track, although its precise origin cannot be easily tracked in the gridded maps of CDOD. Finally, the absence of the onset of significant storms in a range of areocentric solar longitude 250°−310° is also climatologically consistent with what observed in previous years, except for the solstitial planetary-scale event of MY 28 (see the so-called "solstitial pause" mentioned in, e.g., Montabone et al., 2015; Kass et al., 2016; Lewis et al., 2016; Montabone & Forget, 2018; Xiaohua et al., 2019).

Before moving to the analysis of the CDOD diurnal variability, we must consider one last point about the variability of dust storms. When comparing the daily evolution of the GDE and the late winter storm at their early stage in Figs. 11 and 13, they look pretty similar both in intensity and extension. Furthermore, the shapes of the CDOD peaks in the time series of Fig. 10 are also comparable (both positively skewed, with sharp increase and long decreasing tail). What really does make the difference is the fact that a GDE such as the one in MY 34 took about 35 sols of continuous dust injection into the atmosphere to reach a peak in average CDOD that is more than twice as high than the one reached by the (rather intense) late-winter regional storm. This includes a much larger spatial variability during the GDE, as indicated by the root mean square deviation in Fig. 10. An event that was very important in boosting the equinoctial dust storm into the GDE class was the activation of secondary lifting centers in the Tharsis region, which seems to have started around SOY 401 in the gridded maps ($L_S \approx 197°$), and later in the Terra Sabaea region — although one cannot distinguish from the maps whether the increase of optical depth in this region was the result of eastward transport from Tharsis or local dust lifting, or both. Bertrand et al. (2019) highlight this event as well, and analyze it using simulations with the NASA Ames Mars GCM guided by the kriged maps described in this paper. When looking at the CDOD daily evolution in Fig. 12, this Tharsis event can be considered as a "storm within the storm", without which we might have only witnessed a regional storm instead of a GDE. This is one of the reasons why names such as "global dust storm" or "planet-encircling dust storm" do not seem to capture the real nature of this type of extreme events, which are not single storms nor uniquely planet-encircling. Perhaps even "global dust event" is not particularly appropriate, as high latitude regions are mostly free of dust — although indirectly affected by the dust via dynamical effects, but this can be true for regional dust storms as well. One possibility is, therefore, to give these events a name that represents what they really are: "extreme dust events" (EDE).

Another extreme characteristic of the MY 34 equinoctial event is its strong diurnal variability, clearly observed by MCS in the vertical expansion of the dayside vs nightside dusty region (see Kleinböhl et al., 2019), but also featured in the column optical depth values, as already shown in Fig. 4. The time series at different locations extracted from the dataset with four MUT maps per sol and shown in Fig. 14 clearly illustrates this phenomenon. The nightside-dayside variability is different at different locations, but is particularly dramatic in Aonia Terra (to the East of the Argyre Planitia, 90°W−60°W longitude and 60°S−30°S latitude), which is located in the southern latitude band where Kleinböhl et al. (2019) observe strong variability in the dust profiles. In Fig. 15, therefore, we compare the CDOD values in Aonia Terra at two times during the GDE (i.e. during its growth phase and near the peak) with the corresponding dust opacity profiles

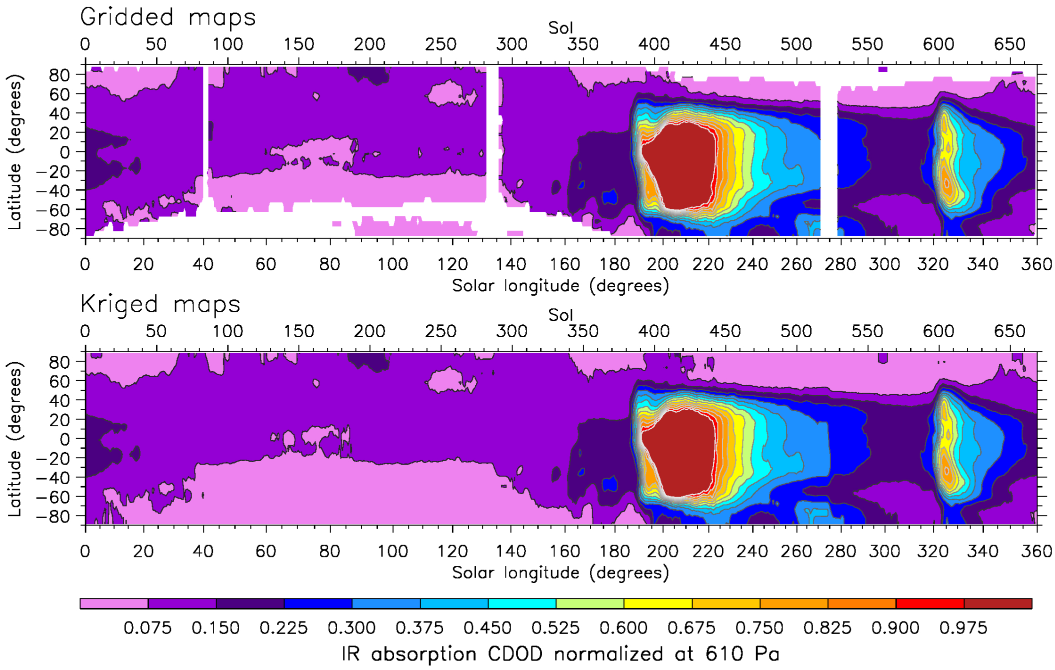

Figure 9. MY 34 latitude vs time plot of the zonally and diurnally averaged gridded maps of 9.3 µm absorption column dust optical depth normalized to the reference pressure level of 610 Pa (upper panel), compared to the same using kriged maps (lower panel). The white color in the upper panel indicates that no valid grid points are available at the corresponding times and latitudes. Kriged maps are complete (all grid points have valid values), therefore no white colour is present in the lower panel.

that are extrapolated and integrated in order to estimate the CDODs. The vertical expansion of about 20 km of the dayside dusty region with respect to the nightside one is quite spectacular at $L_S \approx 207°$, near the peak of the GDE. Unfortunately, with the rise in altitude of the dusty region comes the rise in cut-off altitude of the dust profile retrievals. However, from Fig. 15 one cannot conclude that the homogeneously mixed dust hypothesis at the core of our dust profile extrapolation to the ground does not hold in these cases. Conversely, there is no evidence that rising dust is replaced by more well-mixed dust in the missing part of the profile, because we simply have no data there. Furthermore, uncertainties at the lowest levels of the dust profiles during the GDE tend to be larger (see e.g. left panel of Fig. 1 in Kleinböhl et al., 2019), hence the real shape of the profile in the lowest two scale heights could provide some surprises.

At this point of the analysis, we can make three hypotheses about the diurnal variability observed in MCS CDOD:

1. There is an intrinsic, significant variability of the column dust abundance. In this case, quite a substantial amount of dust must be supplied in the lowest two scale heights during the day, which MCS cannot see through. This extra dust must either be lifted locally from the ground or supplied via horizontal advection (or both). Local mesoscale effects might operate at different locations (e.g. katabatic/anabatic winds, strong convective activity, etc.)
2. There is no significant variability in the column dust abundance. In this case, atmospheric dust is simply moved up and down during the day/night, and the day-

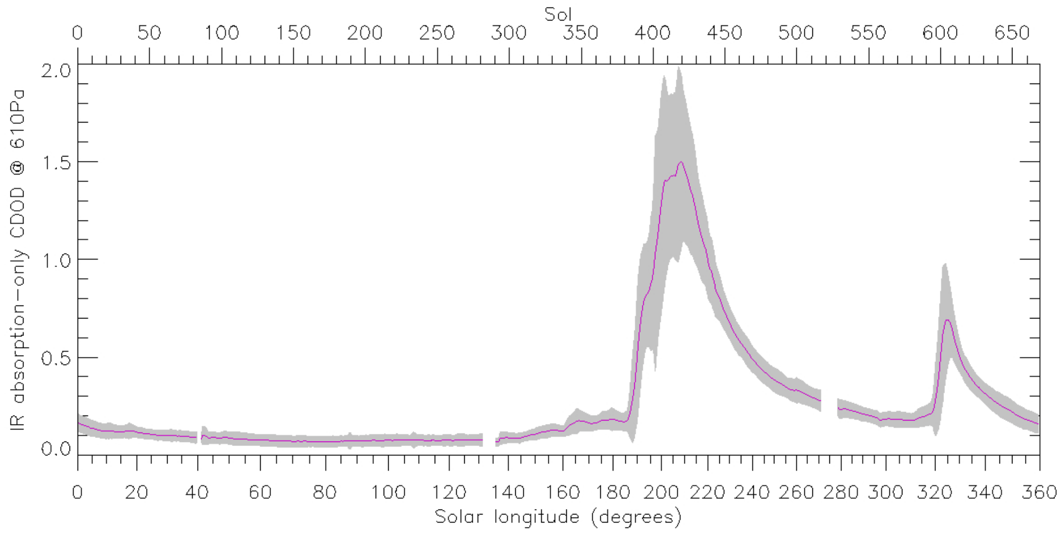

Figure 10. Time series of column dust optical depth (9.3 μm in absorption, normalized to 610 Pa) extracted from the diurnally averaged gridded maps and averaged at all longitude in the latitude band 60°S − 40°N. The grey shade represents the root mean squared deviation, i.e. the spatial variability within the averaged longitudes and latitudes (note that the diurnal variability is not included).

side dust opacities actually decrease with decreasing altitude in the lowest scale heights, which are not seen by MCS. The diurnal variability of the dust opacity profiles in the lowest two scale heights during the GDE would then be expected to be very large, in order to compensate for the vertical expansion of the dust cloud.

3. There is some variability in the column dust abundance. In this case, dust is partly moved up and down at different local times, and partly lifted locally, or advected from nearby locations.

In order to help clarify which hypothesis is more likely, we have carried out simulations with the LMD-GCM, which we discuss in the next section.

4 Global Climate Model simulations of the MY 34 Global Dust Event

The simulations we have carried out using the LMD-MGCM have similar characteristics to those carried out to build the Mars Climate Database version 5.3 (Millour et al., 2015), except for the model top being set lower (at 100 km compared to 250 km, with 29 rather than 49 vertical levels) and the thermospheric parameterizations (González-Galindo et al., 2011) being switched off. The most up-to-date physical parameterizations are included: interactive dust cycle (explained in the next paragraph, Madeleine et al., 2011), thermal plume model (a physically-based parameterization for Planetary Boundary Layer —PBL— mixing, Colaïtis et al., 2013), water cycle with radiative effect of clouds (a key element to account for the measured atmospheric and surface temperatures, Madeleine et al., 2012; Spiga et al., 2017), and full microphysics scheme (in which the transported dust particles could serve as condensation nuclei for the formation of water-ice clouds, Navarro et al., 2014). The "rocket dust storm" parameterization recently built and tested by Wang et al. (2018) is not included in this version of the GCM. The horizontal grid features 64 × 48 longitude-latitude points.

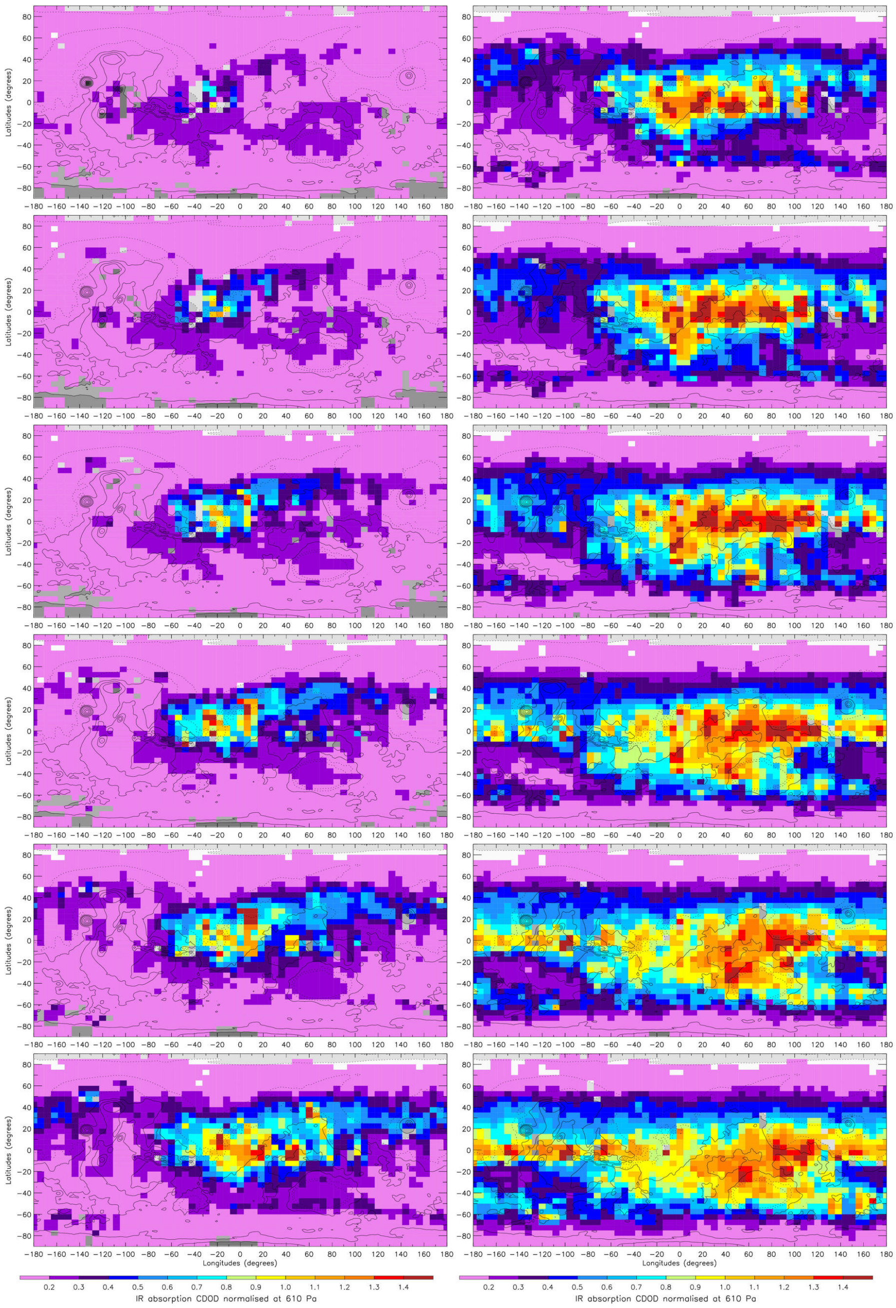

Figure 11. Initial evolution of the MY 34 Global Dust Event. Each panel shows diurnally averaged gridded column dust optical depth (in absorption at 9.3 μm) normalized to the reference pressure level of 610 Pa. From top left to bottom right, maps are provided for (sol-of-year/L_S): 383/186.2°; 384/186.8°; 385/187.4°; 386/188.0°; 387/188.6°; 388/189.2°; 389/189.8°; 390/190.4°; 391/191.0°; 392/191.6°; 393/192.2°; 394/192.8°. L_S is calculated at MUT=12:00 of each sol, and rounded to one decimal place. See also Appendix A of Montabone et al. (2015) for the description of the sol-based Martian calendar we use in this paper.

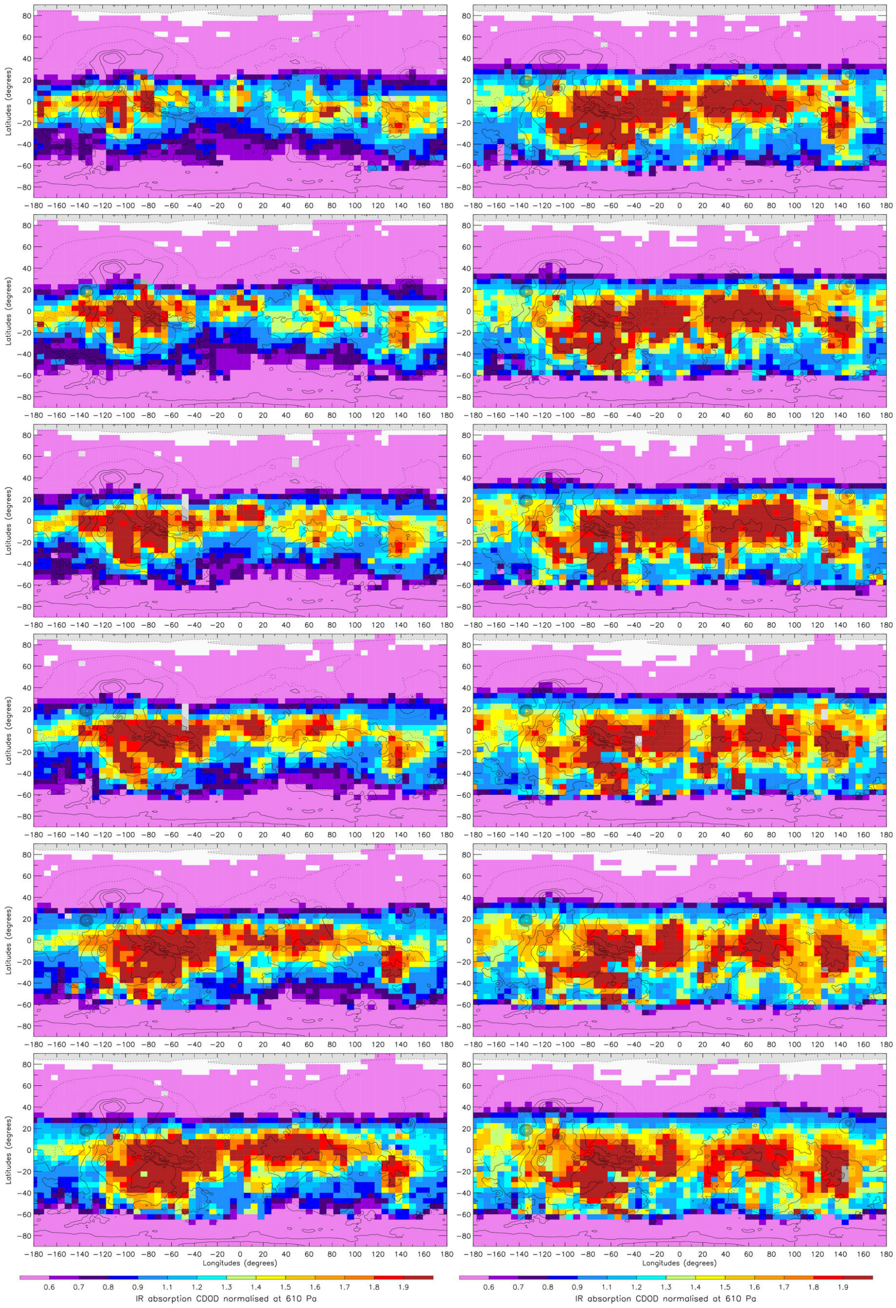

Figure 12. Same as Fig.11 but for the MY 34 secondary storm within the GDE. From top left to bottom right, maps are provided for (sol-of-year/L_S): 401/197.0°; 402/197.6°; 403/198.2°; 404/198.8°; 405/199.4°; 406/200.0°; 407/200.7°; 408/201.3°; 409/201.9°; 410/202.5°; 411/203.1°; 412/203.7°. L_S is calculated at MUT=12:00 of each sol, and rounded to one decimal place. Note that the scale for the CDOD values has changed with respect to Fig. 11.

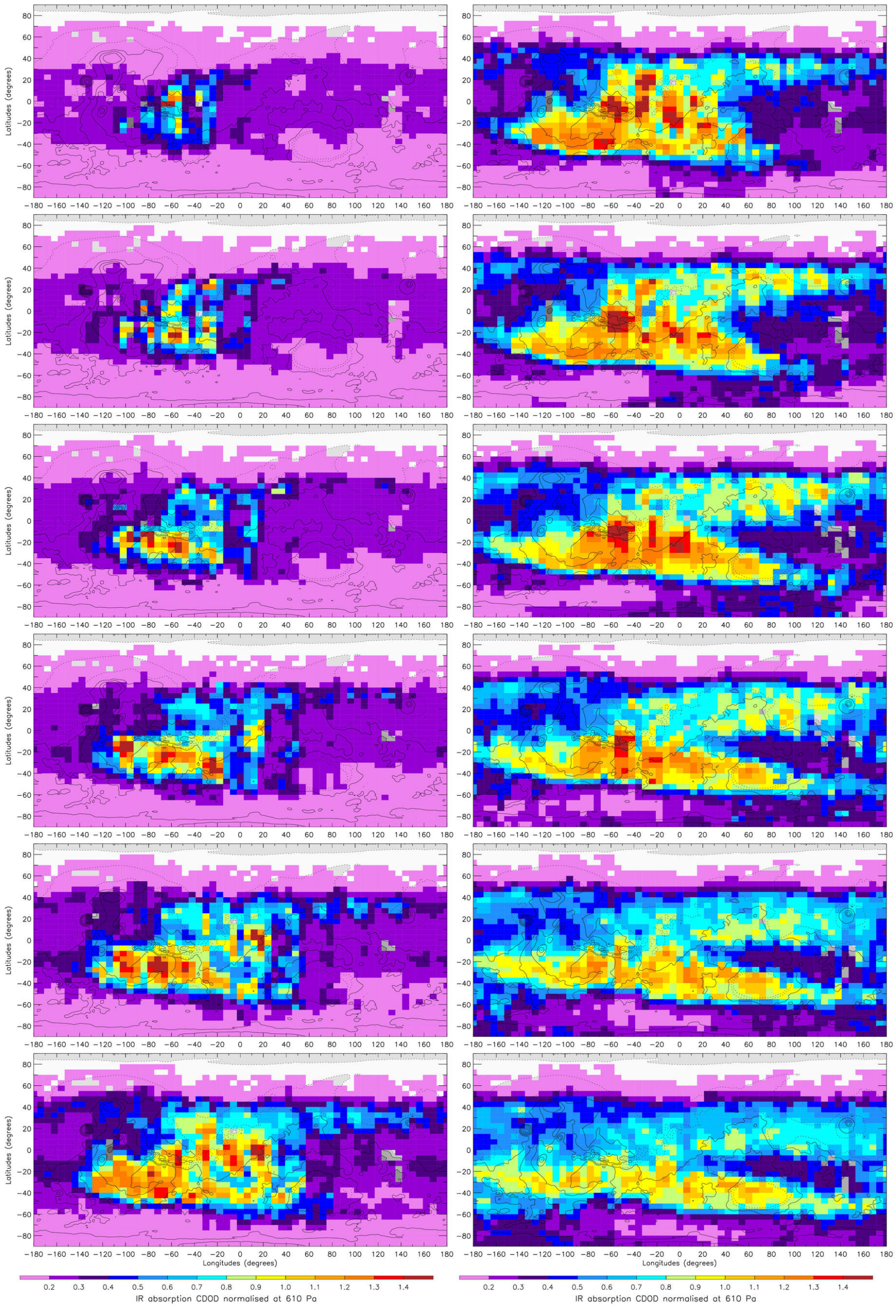

Figure 13. Same as Fig.11 but for the MY 34 late-winter regional storm. From top left to bottom right, maps are provided for (sol-of-year/L_S): 596/320.0°; 597/320.6°; 598/321.2°; 599/321.8°; 600/322.4°; 601/322.9°; 602/323.5°; 603/324.1°; 604/324.7°; 605/325.2°; 606/325.8°; 607/326.4°. L_S is calculated at MUT=12:00 of each sol, and rounded to one decimal place. The scale for the CDOD value is the same as in Fig. 11.

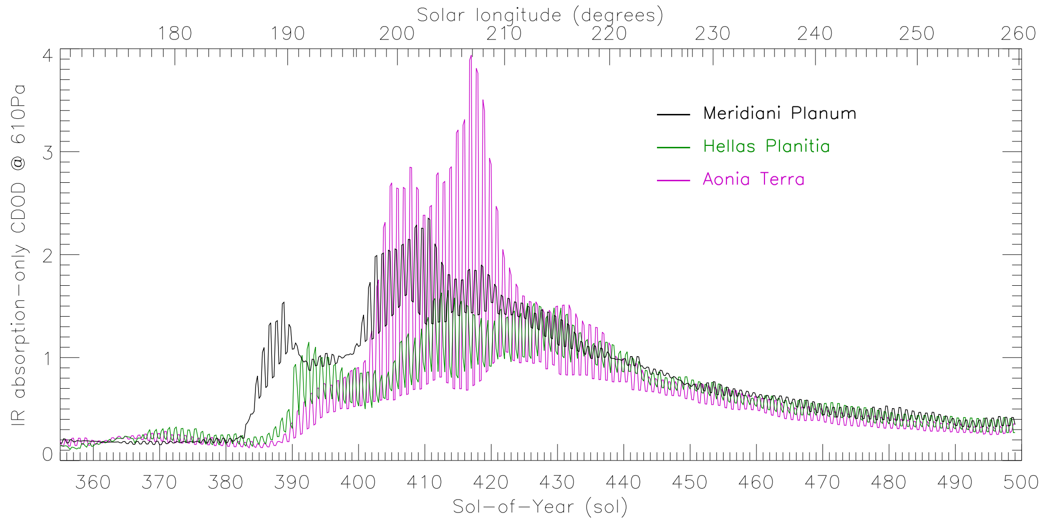

Figure 14. Time series of column dust optical depth (9.3 μm in absorption, normalized to 610 Pa) extracted from the gridded maps with four MUT per sol and spatially averaged in three different areas: Meridiani Planum (15°W − 15°E longitude, 15°S − 15°N latitude), Hellas Planitia (55°E − 85°E longitude, 60°S − 30°S latitude), and Aonia Terra (East of Argyre Planitia: 90°W − 60°W longitude, 60°S − 30°S latitude). The boundaries of the three areas can be visualized as colored squares in the upper panel of Fig. 6. The time series are shown between Sol-of-Year 355 and 500, i.e. $L_S \approx 170° - 260°$.

A complete description of the interactive dust cycle is included in Madeleine et al. (2011) and Spiga et al. (2013). To summarize, the transport of dust particles by the resolved dynamics is based on a two-moment scheme: the particle size distribution is fully described by two tracers (mass mixing ratio and number density) assuming a log-normal distribution of constant standard deviation. When a column-integrated dust scenario (such as the one described herein for MY34) is used in a LMD-GCM run, the value of total column dust opacity is normalized at each timestep by the value in the dust scenario. The vertical distribution of dust particles in the LMD GCM simulation remains a prediction from the model.

A run without the normalization of the total column dust opacity by the value provided in the dust scenario is named a “free-dust” run, since both the column opacity and the vertical distribution of dust particles are fully predicted by the model. For GCM simulations guided by the column-integrated dust scenario, spatially uniform lifting rate is assumed all over the planet, with dust particles being injected in the first layers of the model PBL (Madeleine et al., 2011). Conversely, our “free-dust” run assumes no lifting of dust particles from the surface. Only the normalization of the total column dust opacity, and the lifting of dust particles from the surface, are different between a regular GCM simulation and a “free-dust” simulation. Physical processes such as sedimentation, cloud scavenging, and small-scale mixing of dust particles, are still included in the “free-dust” GCM simulation. The goal of the “free-dust” GCM simulation is thus to clearly identify how the combination of atmospheric dynamics and sinks (sedimentation, cloud scavenging) is acting to modify the spatial distribution of dust particles in the martian atmosphere. This kind of GCM simulation is appropriate for either the clear season, or the decaying phase of dust storms (the latter being the case considered here). During 10 to

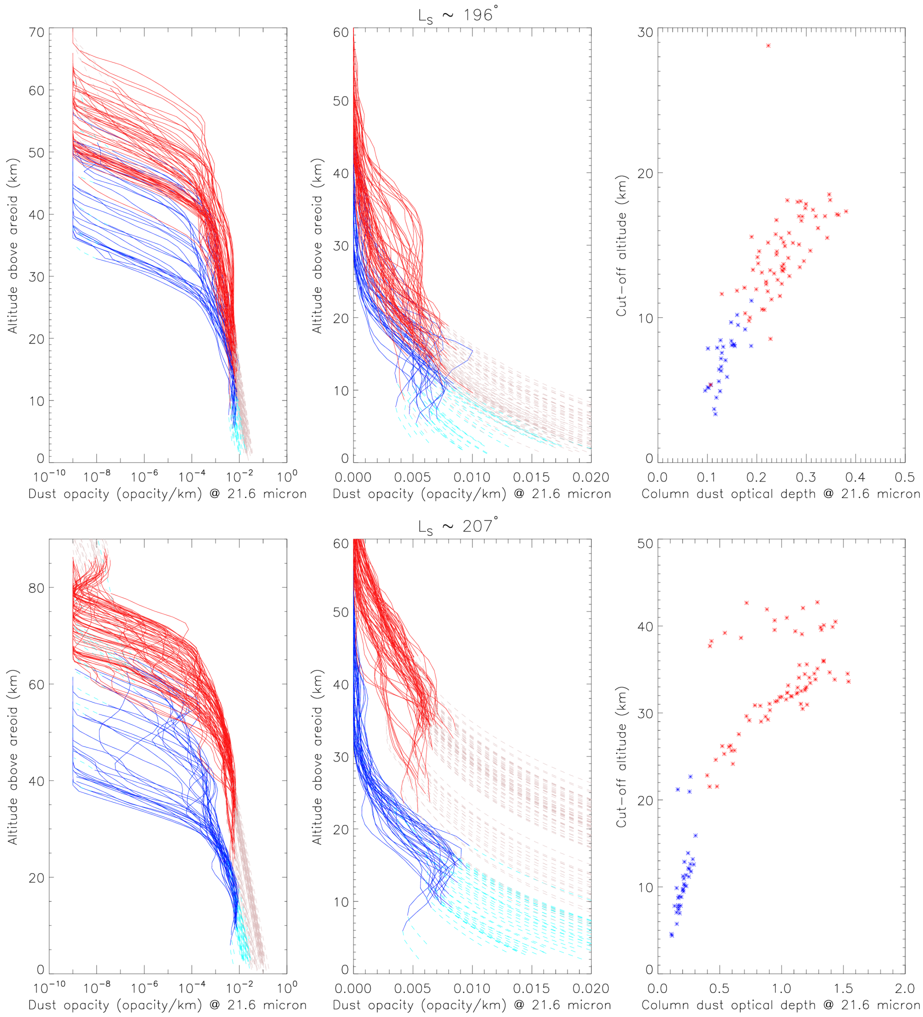

Figure 15. Data plotted in each panel of this figure are for 7 sols centered on either sol-of-year 400 ($L_S \approx 196°$, upper panels) or sol-of-year 418 ($L_S \approx 207°$, lower panels) in Aonia Terra (90°W – 60°W longitude, 60°S – 30°S latitude). Blue indicate nightside data, red is for day-side data. The left and central panels of this figure show the retrieved MCS dust opacity profiles (solid, vivid lines) and the extrapolated sections (dashed, pastel lines) as a function of altitude above the areoid (topography values are interpolated from the MOLA dataset at the corresponding longitudes and latitudes). The x-axis is logarithmic in the left panels, whereas it is linear in the central ones, to better separate the profiles in the lowest scale heights. The right panels show the integrated MCS CDOD in extinction at 21.6 µm (not normalized to 610 Pa) as a function of the cut-off altitudes of their corresponding dust opacity profiles. Note that the x-axis and y-axis ranges can be different among the panels.

20 sols of simulation, the global column opacity predicted by the model does not depart significantly from the global column opacity reported in the dust scenario.

The initial state for the MY 34 run at $L_S = 0°$ uses the "climatological" column-integrated dust scenario typical of MYs devoid of global dust events. Then, two simulations for MY 34 are carried out:

1. a simulation using the reference MY 34 dust scenario v2.5 (i.e. the maps kriged from the diurnally averaged gridded maps, as discussed in Section 2.5) to guide the column dust field throughout the GDE period;
2. a simulation using the MY 34 dust scenario until $L_S = 210°$ (around the peak of the GDE), then continuing as a "free-dust" run for a few sols, with no more external guidance on the column dust field and no more regular injection of dust particles at the bottom of the model, as explained in the previous paragraph.

The LMD-MGCM simulations for MY 34 are also used in Kleinböhl et al. (2019) to discuss the diurnal cycle of the vertical distribution of dust observed by MCS. We use the two types of simulations for two different purposes: 1. the forced run is used to analyse some of the impacts of the MY 34 GDE on the local and global atmospheric dynamics, thus verifying that the use of a diurnally averaged dust scenario produces reasonable results; 2. the "free-dust" run is used to identify possible diurnal variability of the column dust in the model, which could corroborate one of the three hypotheses provided at the end of the last section.

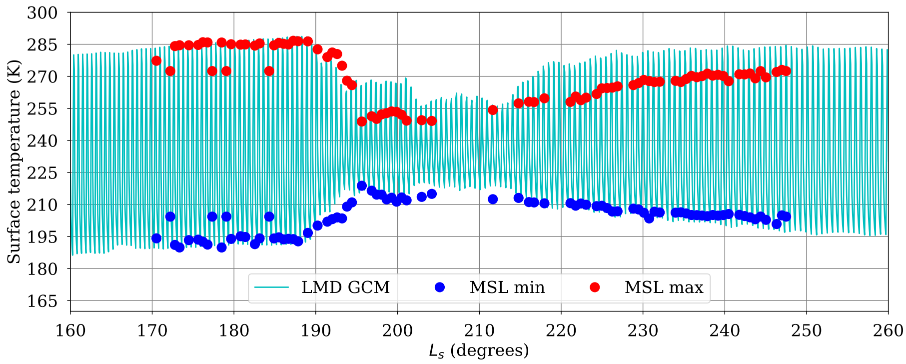

Figure 16. Comparison of surface temperature simulated by the LMD-MGCM model versus surface temperature measured by the Rover Environmental Monitoring Station (REMS) on board MSL "Curiosity" rover (diurnal minimum in blue and diurnal maximum in red). Data from MSL are provided as supplementary material of Guzewich et al. (2019). The model simulation is guided by the column-integrated dust scenario.

Figure 16 shows a comparison between the surface temperature measured by Curiosity (Guzewich et al., 2019) and the surface temperature computed by the LMD-MGCM. When the MY 34 global dust event starts, the diurnal amplitude of temperature is reduced: daytime temperatures are lower as a result of visible absorption of incoming sunlight being more efficient in a dustier atmosphere, and nighttime temperatures are higher as a result of increased infrared radiation emitted towards the surface in a dustier atmosphere. The temporal variability of temperature (absolute and relative values) is well reproduced for the nighttime minimum temperature, but less so for the daytime temperatures (although the qualitative behaviour is correct). There might be three reasons for this: 1. thermal inertia is not well represented in the LMD-MGCM for daytime conditions in Gale Crater; 2. the CDOD observed by MCS in the region of Gale crater is underestimated with respect to the one observed by Curiosity from $L_S \approx 195°$ to $L_S \approx 202°$, and by consequence the corresponding gridded and kriged maps are low-biased at those times (see Fig. 7 in Section 2.6); 3. the accuracy of the calculations by the model radiative transfer could decrease under extreme dust loading conditions, or could be affected by an inaccurate distribution of particle sizes.

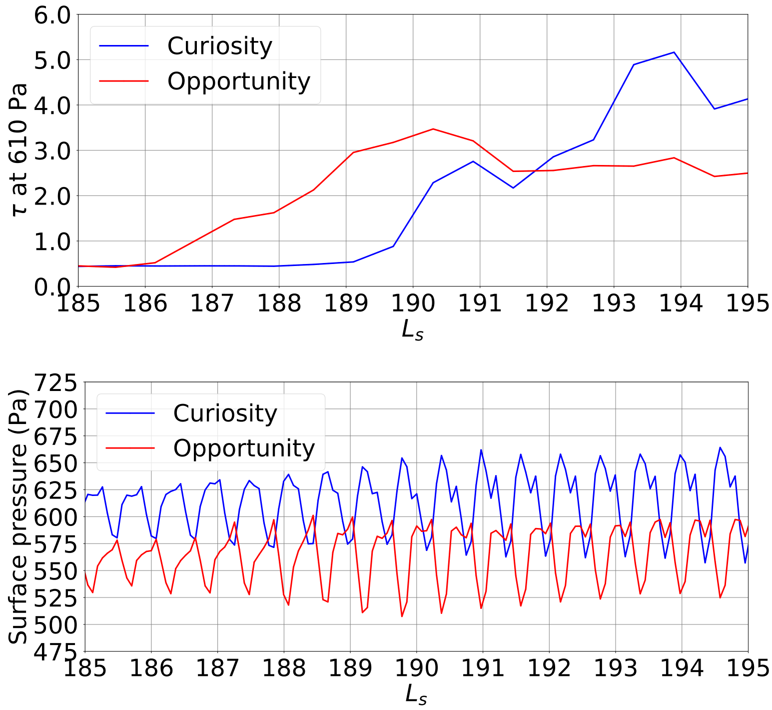

Figure 17. Time series of equivalent-visible column dust optical depth at 610 Pa (upper panel) and surface pressure (lower panel) as simulated by the LMD Mars GCM guided by the MY 34 column-integrated dust scenario. The focus of the figure corresponds to the onset of the GDE. This is showing the simulated fields at the Opportunity (red curves) and Curiosity (blue curves) landing sites.

An important test of the dynamical behavior of our LMD-MGCM simulation forced by the MY 34 column-integrated dust scenario is how thermal tides react to the global increase of dust opacity following the onset of the GDE. Figure 17 shows several diurnal cycles of surface pressure at the time of the GDE onset. Both the amplitude of the diurnal pressure cycle, and its morphology, are modified by the GDE at its onset. The diurnal pressure cycle is dominated by the diurnal tide before the GDE takes place. When the GDE starts to build up and the column optical depth increases, the diurnal mode increases slightly in amplitude while the semi-diurnal mode increases significantly compared to the other modes, as already described in previous studies (Zurek & Martin, 1993; Wilson & Hamilton, 1996; Lewis & Barker, 2005, their Figure 5). The reinforcement of the semi-diurnal tide with increased column opacity is due to the fact that this tide component is dominated by a Hough mode with a large vertical wavelength (Chapman & Lindzen, 1970). As a result, this Hough mode is very sensitive to forcing extended in altitude such as the absorption of incoming sunlight by dust particles during a dust storm.

Those major changes in the tidal modes take only a couple of sols to react to the MY34 GDE onset, and the simulations show that those changes are global. This is true for both the Opportunity site, located close to the regional storm that initiated the MY34 GDE, and the Curiosity site, at which dust opacity started to increase about 5° later than at the Opportunity site. Hence, at the Curiosity site, both the amplification of the diurnal and semi-diurnal modes in the simulated surface pressure are predicted to occur before dust opacity increases locally. This is in agreement with the observations by Curiosity of the diurnal pressure amplitude, which is found to react about 4 sols before the increase of dust opacity observed by Curiosity in Gale Crater (Viúdez-Moreiras et al., 2019).

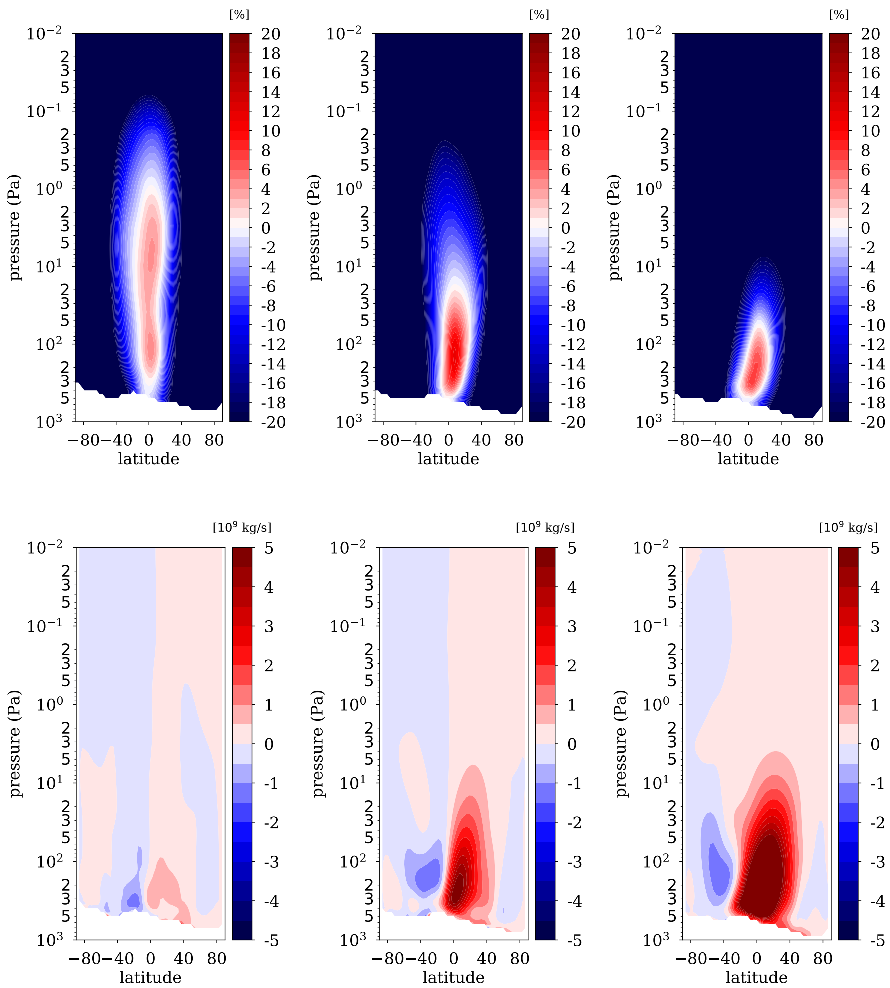

Figure 18. The impact of the MY 34 GDE on the zonally-averaged global circulations on Mars is shown from left to right, averaged on the L_S intervals $150° - 180°$ (pre-GDE conditions), $180° - 210°$ (onset of the GDE), and $210° - 240°$ (mature phase of the GDE). [Top] Super-rotation index s computed according to Lewis & Read (2003) with positive values denoting regions where eastward jets are super-rotating i.e. exceeding the solid-body rotation of the planet. [Bottom] Mass streamfunction with blue regions corresponding to counterclockwise circulation and red regions corresponding to clockwise circulation.

The increase in column dust optical depth associated with the MY 34 GDE has a profound impact on the large-scale circulation. Lewis & Read (2003) evidenced an equatorial low-troposphere super-rotating jet in the atmosphere of Mars, and emphasized the strong positive impact of the atmospheric dust loading on this jet. Our LMD-MGCM forced simulation for MY 34 shows that the intensity of this super-rotating jet, diagnosed by the super-rotation index as in Lewis & Read (2003), is indeed increased following the onset of the GDE from a 5% super-rotation index to a 15% super-rotation index. We also find that this jet becomes confined closer to the surface as the GDE develops (Figure 18, top panels). The mean meridional circulation is also deeply impacted by the large dust loading following the onset of the MY 34 GDE: the intensity of this mean meridional circulation is enhanced by a factor of 10 following the onset and mature phase of the GDE (Figure 18, bottom panels). This behaviour is similar to the evolution of the mean meridional circulation simulated under MY 25 GDE conditions (see e.g. Montabone et al., 2005).

Finally, we discuss the use of a "free dust" simulation to gain some insights on the diurnal variability of CDOD in the GCM model. GCM simulations show that large-scale circulation components (i.e. the mean meridional circulation, planetary waves, and the polar vortex) cause the vertical distribution of dust to undergo diurnal variations both in equatorial and extratropical regions (Kleinböhl et al., 2019). Figure 19 shows the column dust optical depth simulated in the free-dust LMD-MGCM run after $L_S = 210°$ (i.e. near the peak of the MY 34 storm). The total column optical depth freely evolves in the simulation without being normalized using the values in the MY 34 column-integrated dust scenario. As observed in the MCS CDOD values, and by consequence in the gridded/kriged maps reconstructed following the method described in this paper, the column optical depth in the "free dust" model run varies significantly on a diurnal basis in some regions. Figure 20 shows that the modeled diurnal anomalies in visible column dust optical depth can reach about $\overline{\tau}\pm1.5$ in specific regions – particularly Aonia Terra, as observed in the estimates for MCS CDODs. It also clearly shows that a strong wavenumber-1 wave is present at mid-latitudes in the southern hemisphere, which coincides with what is observed for instance in Fig. 5. Furthermore, when looking at anomaly maps for more than one sol, they also show that baroclinic waves are present at low latitudes in the northern hemisphere, thus explaining the variability at other locations (not shown here).

The diurnal variability of the CDOD reproduced by the model results from horizontal transport by the large-scale circulation. To diagnose this, and to rule out the influence of sinks of dust particles still included in the "free dust" GCM simulation, such as sedimentation and cloud scavenging, the temporal change $\partial q/\partial t$ of dust mass mixing ratio q can be compared to the divergence $\nabla \cdot (q\vec{v})$, which represents the horizontal flux of dust particles transported by the horizontal wind $\vec{v}$. Under the assumption that the wind transport of dust particles dominates the sinks, the two terms should be strongly correlated since the horizontal transport is simply governed by a conservation law, which states:

$$\frac{\partial q}{\partial t} + \nabla \cdot (q\vec{v}) = 0.$$

Figure 21 provides a mapping of the two terms, along with wind vectors, at an altitude where the diurnal contrasts in dust mixing ratio are particularly strong (see Figure 15). At every local time in a sol, the divergence term and the temporal term are closely related. Especially in the southern hemisphere, the diurnal cycle of atmospheric circulations — notably the thermal tides amplified by the dust storm conditions — cause a significant diurnal cycle of horizontal transport of dust particles, hence an overall diurnal cycle of the column opacity at particular locations (such as Aonia Terra exemplified previously). Through the horizontal transport of dust particles, daytime regions are a "source" of dust particles, while nighttime regions are a "sink" of dust particles. Hence, in this study, we show that a diurnal cycle of column opacity is associated with the diurnal cycle of vertical distribution of dust particles evidenced in Kleinböhl et al. (2019).

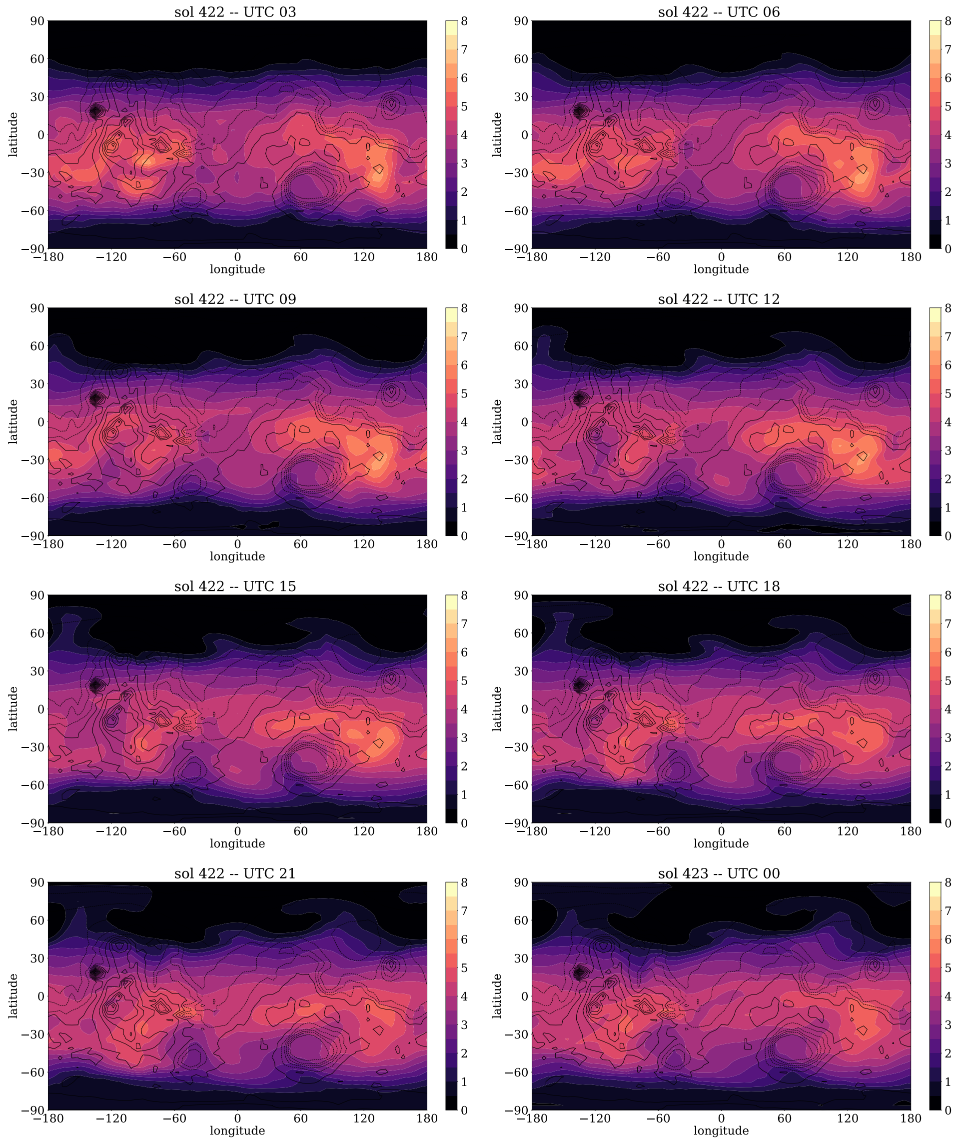

Figure 19. Sequence of column dust optical depth maps separated by 3 hours over one sol in a LMD-MGCM "free dust" simulation where, contrary to the simulation guided by the MY 34 column-integrated dust scenario, the dust mass mixing ratio in the model is not normalized to match the total column dust optical depth of the scenario. This "free dust" simulation was restarted from the simulated state of the atmosphere at $L_S = 210°$ in a regular LMD-MGCM simulation guided by the MY 34 dust scenario.

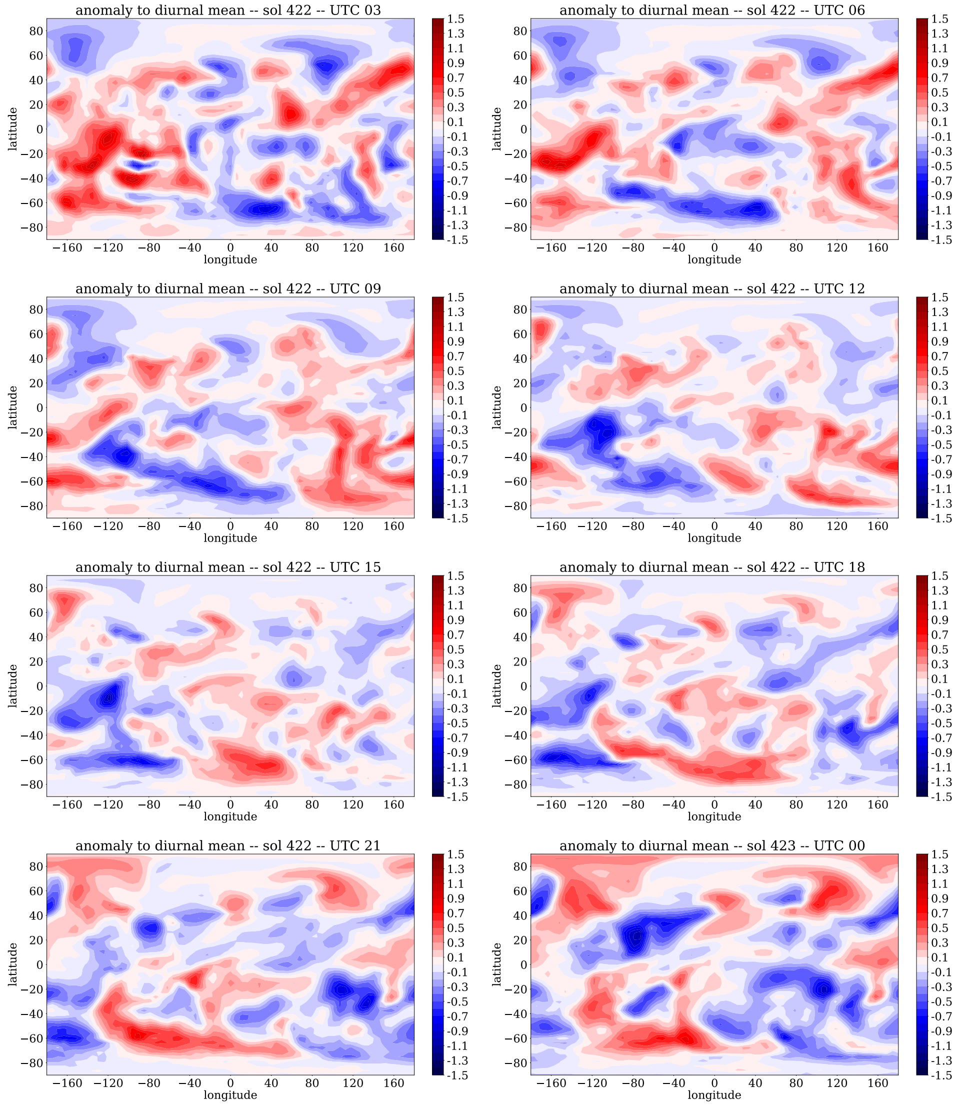

Figure 20. Same as Figure 19 except that the anomaly relative to the diurnal mean is shown.

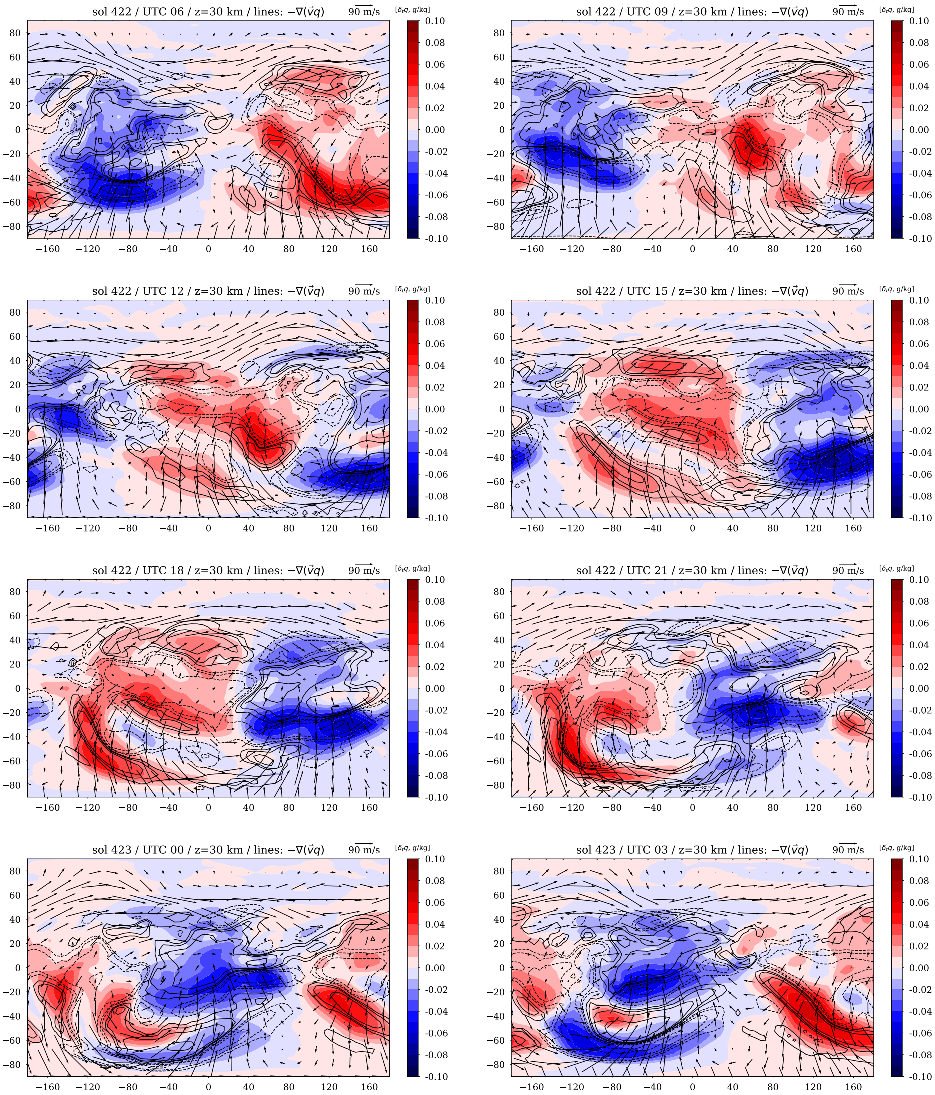

Figure 21. Sequence of maps separated by 3 hours over one sol in a LMD-MGCM "free dust" simulation (see the caption of Figure 19). Colors depict the temporal variation of dust mass mixing ratio q within a time interval corresponding to the considered local time ± 3 hours. Lines depict the horizontal divergence of dust flux $q\vec{v}$, i.e. the horizontal transport of dust particles. The horizontal wind vectors $\vec{v}$ are superimposed. Note that the first panel (top left) is at 06:00 MUT because the temporal derivative uses data from the previous output at 03:00 MUT.

While it is not possible to rule out the other possible interpretations for the observed diurnal variability of column dust optical depth as discussed at the end of Section 3, the LMD-MGCM results in Figure 19 strongly suggest that this variability has a physical basis, and at least part of it is likely related to the large-scale horizontal transport. Vertical transport also likely plays a central role, as discussed in Kleinböhl et al. (2019). What our GCM simulation cannot tell, however, is how much specific mesoscale phenomena, including dusty deep convection (i.e. "rocket dust storms", Spiga et al., 2013), or PBL processes, contribute to the stronger diurnal variability observed by MCS.

5 Conclusions and remarks

The work described in this paper was devoted to 1. reconstructing maps of column dust optical depth for MY 34 from Mars Reconnaissance Orbiter/Mars Climate Sounder observations, 2. analyzing the seasonal, daily, and diurnal variability of column dust showed by the maps, and 3. using numerical simulations with the Laboratoire de Météorologie Dynamique Mars Global Climate Model, forced by or simply initiated with the reconstructed CDOD maps, in order to examine some aspects of the impact of the MY 34 global dust event on local and global scale atmospheric dynamics, including the diurnal variability of column dust.

The reconstructed maps for MY 34 follow the work by Montabone et al. (2015) and extend the publicly available multi-annual, multi-instrument climatology of column dust optical depth to 11 Martian years. An important difference of the present work with respect to Montabone et al. (2015) is that we now reconstruct diurnally-varying maps of column dust, which provides access to the analysis of the diurnal variability of this quantity. This is made possible by using novel retrievals (version 5.3.2) of dust opacity profiles from MCS observations during the period May 21, 2018, to October 15, 2018 ($L_S = 179° - 269°$ in MY 34), which extend lower in altitude than standard version 5.2 retrievals. In general, therefore, the estimated column dust optical depth values during the global dust event of MY 34 are more accurate, within the intrinsic limitations of estimating CDODs from limb observations.

The analysis of the MY 34 column dust variability at different temporal scales using the reconstructed maps highlights that:

- MY 34 reproduces the dichotomy observed in the 10 previous years between the "low dust loading" and the "high dust loading" seasons. Note that MY 35, which started in March 2019, features an unusual regional dust storm during the LDL season at $L_S \approx 35°$ (D. Kass, personal communication). However, its intensity and duration, preliminarily estimated from CDOD maps using MCS observations, are still compatible with the concept of a "low dust loading" season;
- It also features other typical characteristics of the seasonal evolution of CDOD, such as large values at southern polar latitudes peaking at $L_S \approx 270°$, a solstitial pause in a L_S range $250° - 310°$, and large values peaking again at $L_S \approx 325°$ during the evolution of an intense late-winter regional dust storm;
- The key distinction of MY 34 is undoubtedly the equinoctial global dust event (starting at $L_S \approx 186°$ only a few sols after the equivalent event in MY 25), which seems to feature a "storm within the storm" at $L_S \approx 197°$, boosting its growth to attain extreme characteristics, typical of GDEs;
- The MY 34 GDE seems also to feature very large CDOD diurnal variability at selected locations, particularly at southern mid- and high-latitudes, as already observed in the corresponding MCS dust opacity profiles by Kleinböhl et al. (2019).

While the diurnal variability in dust opacity profiles comes from direct MCS retrievals, and could be explained by global climate model simulations invoking the effects of the large-scale circulation (Kleinböhl et al., 2019), the diurnal variability in the indirectly estimated column dust optical depth values poses more challenging questions. Is the diurnal variability intrinsic to the column dust, or should we expect that the shape of the dust profile in the lowest one or two scale heights not directly observed by MCS (particularly in dayside observations) is not compatible with a homogeneously mixed assumption? Whether the answer leans towards the former or the latter, or a bit of both, it would provide new knowledge on how dust is three-dimensionally distributed within Martian dust storms.

It is not the purpose of this paper to provide a definite answer to the aforementioned question. Nevertheless, we have resorted to numerical simulations with the LMD-MGCM to provide us with some hints. Using a "free dust" model run, initiated at $L_S = 210°$ with the reconstructed CDOD field, the model is able to reproduce some diurnal variability in column dust at selected locations. Despite the fact that both the range of the variability and the precise locations do not coincide with what is estimated from MCS, this result provides physical evidence that some degree of diurnal variability can be expected not only in the upper portion of the dust profiles but also in the whole columns. Furthermore, the dust lifting and PBL parameterizations of the global model might actually miss some of the important features that lead to an accurate description of the three-dimensional dust distribution. The model result might, therefore, underestimate the real variability of the column dust.

What the model simulations clearly show when forced with diurnally averaged CDOD maps, however, is that the impact of the MY 34 GDE on the atmospheric dynamics is as large as for the MY 25 GDE. Key features of the local and global dynamics (such as tides, mean meridional circulation, and equatorial winds) respond to the equinoctial dust events in a very similar manner. This is also an indirect validation of the MY 34 reference column-integrated dust scenario based on the diurnally averaged CDOD maps from MCS, which is currently used in several modeling studies of the 2018 GDE.

Future work should address the possibility of producing diurnally-varying (complete) kriged maps from the diurnally-varying (incomplete) gridded ones, and making them publicly available. As mentioned in Subsection 2.5, we consider that this option is not currently viable, mainly because the CDOD diurnal variability is not yet independently confirmed, and because it is not yet clear whether model simulations forced by a diurnally-varying, column-integrated dust scenario are free of spurious effects. Current Mars GCMs might need to be adapted to handle diurnally varying CDODs in a stable and sensible fashion, if the degree of variability is proved to be as large as the one shown in this paper. A further technical issue that complicates the production of diurnally-varying kriged maps is that some of the gridded maps have many missing values (particularly when the water ice opacity affects the dust opacity), hence some assumptions are required before applying the spatial interpolation. In the present work, we have bypassed this issue by diurnally averaging the gridded maps before producing the kriged ones. A future option could also be the production of fully three-dimensional maps, based on the values of dust opacity at different pressures rather than on the column-integrated values.

Strong emphasis should also be put on obtaining future observations of column-integrated dust as well as dust profiles with diurnal frequency. The Planetary Fourier Spectrometer (PFS) aboard Mars Express, and the Atmospheric Chemistry Suite (ACS) aboard Trace Gas Orbiter currently provide the capability to retrieve CDOD at multiple local times, and could help in the comparison with the estimated MCS day-night variability of column dust. Future observations from the forthcoming Emirates Mars Mission (EMM) might provide even stronger evidence of the presence or absence of diurnal variability, due to the spacecraft coverage of multiple local times at once at apoapsis (when the spacecraft is able to observe the full Martian disk).

Moreover, novel approaches should be taken in the future, in order to fully characterize the diurnal cycle of dust and accurately monitor the evolution of dust storms on Mars. These include:

- the use of satellites in Mars-stationary orbits (also called "areostationary"), which are equatorial, circular, planet-synchronous orbits equivalent to geostationary ones for the Earth (see e.g. Montabone et al., 2018);
- the use of instruments that allow observation of the vertical distribution of the dust in the Martian PBL, such as lidars. This is particularly important during dust storms when IR spectrometers/radiometers (both nadir- and limb-looking) fail to produce reliable retrievals because of the large atmospheric opacity and the reduced temperature contrast. In this paper we have in fact shown that it would be quite critical to know whether the assumption of homogeneously mixed dust still holds in the lowest scale heights in the midst of a dust storm.

Appendix A MY 34 dust climatology versioning

MCS version 5.3.2 is an interim, experimental version of retrievals, leading to a possible future improved version of the whole MCS dataset. As a consequence, the MY 34 gridded and kriged datasets should be considered work in progress, as should the datasets related to other Martian years. It is our intention to regularly update the multi-annual, multi-instrument dust climatology with new observations, novel retrievals of past observations, and updated gridding methodologies/features. The updates are likely to be made publicly available on the Mars Climate Database project webpage at the URL `http://www-mars.lmd.jussieu.fr/`. There exist, therefore, multiple versions of these reference dust climatologies, notably for MY 34, and we would like to provide in this appendix some details about the main differences.

As mentioned in Section 2, the reference version of the current maps from MY 24 to 32 is v2.0. For this version, the used gridding/kriging methodology is precisely the one described in Montabone et al. (2015). Version 2.1 is a specific version only for MY 33, where we have used an additional weight for THEMIS observations, in order to account for THEMIS retrievals being provided at progressively later local times (i.e. we apply a 0.5 weight to THEMIS CDODs during the first iteration with the time window of 1 sol, reduced to 0.1 for the subsequent iterations using larger time windows). Since v2.1 we have also started using MCS v5.2 "two-dimensional" retrievals (Kleinböhl et al., 2017a) instead of v4.3 "one-dimensional" retrievals used for previous years 28 to 32.

For MY 34, we have produced three intermediate versions (v2.2, v2.3, and v2.4) and the v2.5 described in this paper, which should be considered as the reference version. All three intermediate versions use MCS v5.3.2 retrievals for the available period, and MCS v5.2 for the rest of the time, but do not use the two distinctive features described in Subsection 2.4, namely the local time cut-off window of ± 7 hours for observations considered for the weighted average at each grid point, and the 6 hour moving average producing 4 maps per sol. Instead, they use observations at all local times for each grid point (except in v2.3 and v2.4 during the GDE, see below), and the 24 h moving average produces only one map per sol, centered at MUT=12:00, as described in Montabone et al. (2015).

Within the intermediate versions, the differences are as following:

- v2.2: This version still uses the same data QC and gridding methodology as in Montabone et al. (2015). The use of dayside values is limited by the application of the "dayside" filter with 8 km cut-off altitude threshold at any time. Apart the use of MCS v5.3.2 retrievals, the only other difference with respect to v2.0 is in the kriged maps, where we have artificially introduced climatological south cap edge "storm" only for areocentric solar longitude earlier than 180°, as in MY 25. This version also uses MCS observations only until end of September 2018 ($L_S \approx 260°$), stopping at SOY 501.

- v2.3: This version uses only dayside values during the GDE ($186.5° < L_S < 269°$, SOY 383 to 515). It has also an improved data QC with respect to v2.2: we introduced the "water ice" filter, the "cross-track" filter, and we did not apply the "dayside filter" with 8 km cut-off altitude threshold during the GDE and the late winter regional storm ($L_S > 312°$). This allowed to use many more dayside values during the two major dust events of MY 34, increasing the overall optical depth to levels observed by, e.g., the Opportunity rover. We also redefined the estimation of uncertainties according to the scheme that was later adopted in v2.5 (but with slightly lower uncertainties overall). Furthermore, we changed a couple of parameters in the IWB methodology: the criterion to accept a value of weighted average at a particular grid point at any given iteration became that there must be at least one observation within a distance of 200 km from the grid point. We started using the same surface pressure recorded in the MCS dataset to normalize CDOD to 610 Pa, instead of the MCD surface pressure. If MCS surface pressure is not retrieved, we associated a 10% uncertainty by default. We stopped using the artificial modification of a latitude band around the southern polar cap at all times. This version also uses MCS observations only until end of February 2018 ($L_S \approx 349°$), stopping at SOY 647.
- v2.4: This version is quite similar to v2.3. The only differences are in the refined data QC, which is the one we also use in v2.5 (see Subsection 2.2). It also extends until the end of MY 34.

Refer to the two Figures in the Supplementary Information for a comparison of results using versions 2.2, 2.3, 2.4 and 2.5.

Data availability

The maps of gridded and kriged CDOD produced in this work are publicly available on the "Institut Pierre-Simon Laplace" (IPSL) data repository (accessible via the URL `https://doi.org/10.14768/20191217001.1`). The available datasets include the diurnally-averaged gridded and kriged maps (reference column dust climatology, version 2.5), and the sub-daily gridded maps (version 2.5.1). The same maps are available under the Mars Climate Database project webpage (at the current URL `http://www-mars.lmd.jussieu.fr/mars/dust_climatology/`). Mars Climate Sounder data is publicly available on NASA's Planetary Data System (`https://pds-atmospheres.nmsu.edu/`). Data from Curiosity rover obtained by the Rover Environmental Monitoring Station (REMS) instrument is publicly available as supplementary material of Guzewich et al. (2019). GCM outputs and supporting Python scripts used to produce the figures related to modeling results are provided in the Supplementary Information of this paper.

Acknowledgments

The work related to the production of reconstructed gridded and kriged CDOD maps for MY 34 is funded by the French Centre National d'Etudes Spatiales (CNES). This work uses technical achievements and expertise obtained during a parallel project of improving the gridding of column dust optical depth retrievals from satellite observations, funded by NASA PDART program (Grant no. NNX15AN06G).

Work related to MCS observations and retrievals (including the estimates of CDOD) is carried out at the Jet Propulsion Laboratory, California Institute of Technology, and is performed under a contract with NASA. Government sponsorship is acknowledged.

The GCM simulations were performed using HPC resources of CINES (GENCI Grant 2019-A0060110391).

The authors wish to thank R. John Wilson for useful comments on early versions of the reference MY 34 dust climatology datasets as well as two anonymous reviewers and JGR Associate Editor Claire E. Newman for insightful suggestions that helped a lot to improve the manuscript. They also thank the data center ESPRI/IPSL for hosting the MY 34 column dust datasets, and for providing help in making the data publicly available.

Luca Montabone wishes to dedicate this work to his father Augusto, who started his journey to the stars during the production of this paper.

References

Bertrand, T., Wilson, R. J., Kahre, M. A., Uratal, R., & Kling, A. (2019). Simulation of the 2018 global dust storm on mars using the nasa ames mars gcm: A multi-tracer approach. *Journal of Geophysical Research - Planets*, *125*(7). doi: 10.1029/2019JE006122

Cantor, B. A. (2007). MOC observations of the 2001 Mars planet-encircling dust storm. *Icarus*, *186*, 60-96. doi: 10.1016/j.icarus.2006.08.019

Chapman, S., & Lindzen, R. (1970). *Atmospheric tides. Thermal and gravitational.* Dordrecht: Reidel, 1970.

Colaïtis, A., Spiga, A., Hourdin, F., Rio, C., Forget, F., & Millour, E. (2013). A thermal plume model for the Martian convective boundary layer. *Journal of Geophysical Research (Planets)*, *118*, 1468-1487. doi: 10.1002/jgre.20104

Fedorova, A., Bertaux, J.-L., Betsis, D., Montmessin, F., Korablev, O., Maltagliati, L., & Clarke, J. (2018). Water vapor in the middle atmosphere of Mars during the 2007 global dust storm. *Icarus*, *300*, 440-457. doi: 10.1016/j.icarus.2017.09.025

Forget, F., Spiga, A., Dolla, B., Vinatier, S., Melchiorri, R., Drossart, P., ... Gondet, B. (2007). Remote sensing of surface pressure on Mars with the Mars Express/OMEGA spectrometer: 1. Retrieval method. *Journal of Geophysical Research (Planets)*, *112*(E11), 8-+. doi: 10.1029/2006JE002871

Girazian, Z., Luppen, Z., Morgan, D. D., Chu, F., Montabone, L., Thiemann, E. M. B., ... Němec, F. (2019). Variations in the ionospheric peak altitude at mars in response to dust storms: 13 years of observations from the mars express radar sounder. *Journal of Geophysical Research - Space Physics*, accepted.

González-Galindo, F., Määttänen, A., Forget, F., & Spiga, A. (2011). The martian mesosphere as revealed by co2 clouds observations and general circulation modeling. *Icarus*, *216*, 10-22.

Guzewich, S. D., Lemmon, M., Smith, C. L., Martínez, G., de Vicente-Retortillo, Á., Newman, C. E., ... Zorzano Mier, M.-P. (2019). Mars Science Laboratory Observations of the 2018/Mars Year 34 Global Dust Storm. *Geophysical Research Letters*, *46*(1), 71-79. doi: 10.1029/2018GL080839

Heavens, N. G., Kleinböhl, A., Chaffin, M. S., Halekas, J. S., Kass, D. M., Hayne, P. O., ... Schofield, J. T. (2018). Hydrogen escape from Mars enhanced by deep convection in dust storms. *Nature Astronomy*, *2*, 126-132. doi: 10.1038/s41550-017-0353-4

Hernández-Bernal, J., Sánchez-Lavega, A., del Río-Gaztelurrutia, T., Hueso, R., Cardesín-Moinelo, A., Ravanis, E. M., ... Wood, S. (2019). The 2018 martian global dust storm over the south polar region studied with mex/vmc. *Geophysical Research Letters*, *46*(17-18), 10330-10337. doi: 10.1029/2019GL084266

Kahre, M. A., Murphy, J. R., Newman, C. E., Wilson, R. J., Cantor, B. A., Lemmon, M. T., & Wolff, M. J. (2017). The Mars Dust Cycle. In *The atmosphere and climate of mars, edited by r.m. haberle et al. isbn: 9781139060172. cambridge* *university press, 2017, p. 229-294* (p. 229-294). doi: 10.1017/9781139060172.010

Kass, D., Schofield, J., Kleinböhl, A., McCleese, D., Heavens, N., Shirley, J., & Steele, L. (2019). Mars climate sounder observation of mars' 2018 global dust storm. *Geophysical Research Letters*, *0*(ja). doi: 10.1029/2019GL083931

Kass, D. M., Kleinböhl, A., McCleese, D. J., Schofield, J. T., & Smith, M. D. (2016, Jun). Interannual similarity in the Martian atmosphere during the dust storm season. *Geophysical Research Letters*, *43*(12), 6111-6118. doi: 10.1002/2016GL068978

Kleinböhl, A., Chen, L., & Schofield, J. T. (2017b, January). Far Infrared Spectroscopic Parameters of Mars Atmospheric Aerosols and their Application to MCS Retrievals in High Aerosol Conditions. In F. Forget & M. Millour (Eds.), *The mars atmosphere: Modelling and observation* (p. 2230).

Kleinböhl, A., John Wilson, R., Kass, D., Schofield, J. T., & McCleese, D. J. (2013, May). The semidiurnal tide in the middle atmosphere of Mars. *Geophysical Research Letters*, *40*(10), 1952-1959. doi: 10.1002/grl.50497

Kleinböhl, A., Schofield, J. T., Abdou, W. A., Irwin, P. G. J., & de Kok, R. J. (2011). A single-scattering approximation for infrared radiative transfer in limb geometry in the Martian atmosphere. *J. Quant. Spectrosc. Rad. Transfer*, *112*, 1568-1580.

Kleinböhl, A., Schofield, J. T., Kass, D. M., Abdou, W. A., Backus, C. R., Sen, B., … McCleese, D. J. (2009, October). Mars Climate Sounder limb profile retrieval of atmospheric temperature, pressure, and dust and water ice opacity. *Journal of Geophysical Research (Planets)*, *114*, 10006. doi: 10.1029/2009JE003358

Kleinböhl, A., Spiga, A., Kass, D. M., Shirley, J. H., Millour, E., Montabone, L., & Forget, F. (2019). Diurnal variations of dust during the 2018 global dust storm observed by the mars climate sounder. *Journal of Geophysical Research - Planets*, accepted. doi: 10.1029/2019JE006115

Kleinböhl, A., Friedson, A. J., & Schofield, J. T. (2017a). Two-dimensional radiative transfer for the retrieval of limb emission measurements in the martian atmosphere. *Journal of Quantitative Spectroscopy and Radiative Transfer*, *187*, 511 - 522. doi: https://doi.org/10.1016/j.jqsrt.2016.07.009

Levine, J. S., Winterhalter, D., & Kerschmann, R. L. (2018). *Dust in the atmosphere of mars and its impact on human exploration.* Cambridge Scholars Publishing, UK.

Lewis, S. R., & Barker, P. R. (2005). Atmospheric tides in a Mars general circulation model with data assimilation. *Advances in Space Research*, *36*, 2162-2168. doi: 10.1016/j.asr.2005.05.122

Lewis, S. R., Mulholland, D. P., Read, P. L., Montabone, L., Wilson, R. J., & Smith, M. D. (2016). The solsticial pause on Mars: 1. A planetary wave reanalysis. *Icarus*, *264*, 456-464. doi: 10.1016/j.icarus.2015.08.039

Lewis, S. R., & Read, P. L. (2003). Equatorial jets in the dusty Martian atmosphere. *Journal of Geophysical Research (Planets)*, *108*, 5034-+. doi: 10.1029/2002JE001933

Madeleine, J.-B., Forget, F., Millour, E., Montabone, L., & Wolff, M. J. (2011, November). Revisiting the radiative impact of dust on Mars using the LMD Global Climate Model. *Journal of Geophysical Research (Planets)*, *116*, 11010. doi: 10.1029/2011JE003855

Madeleine, J.-B., Forget, F., Millour, E., Navarro, T., & Spiga, A. (2012). The influence of radiatively active water ice clouds on the Martian climate. *Geophys. Res. Lett.*, *39*, 23202. doi: 10.1029/2012GL053564

Malin, M. C., Cantor, B. A., & W., B. A. (2018). *Mro marci weather report for the week of 4 june 2018 – 10 june 2018.* Malin Space Science Systems Captioned Image Release, MSSS-534, `http://www.msss.com/msss_images/2018/06/13/`.

Martin, L. J., & Zurek, R. W. (1993). An analysis of the history of dust activity on

Mars. *J. Geophys. Res.*, *98*(E2), 3221-3246.

McCleese, D. J., Schofield, J. T., Taylor, F. W., Calcutt, S. B., Foote, M. C., Kass, D. M., … Zurek, R. W. (2007). Mars Climate Sounder: An investigation of thermal and water vapor structure, dust and condensate distributions in the atmosphere, and energy balance of the polar regions. *Journal of Geophysical Research (Planets)*, *112*(E11), 5-+. doi: 10.1029/2006JE002790

Millour, E., Forget, F., Spiga, A., Navarro, T., Madeleine, J.-B., Montabone, L., … MCD/GCM development Team (2015). The Mars Climate Database (MCD version 5.2). *European Planetary Science Congress 2015*, *10*, EPSC2015-438.

Montabone, L., & Forget, F. (2018). Forecasting Dust Storms on Mars: a Short Review. In *Dust in the atmosphere of mars and its impact on human exploration* (p. 000). Cambridge Scholars Publishing, Ed. Levine, G. S. and Winterhalter, D. and Kerschmann, R. L. doi: doi_tbd

Montabone, L., Forget, F., Millour, E., Wilson, R. J., Lewis, S. R., Cantor, B., … Wolff, M. J. (2015). Eight-year climatology of dust optical depth on Mars. *Icarus*, *251*, 65-95. doi: 10.1016/j.icarus.2014.12.034

Montabone, L., Forget, F., Smith, M., Cantor, B., Wolff, M., Capderou, M., & Van-Woerkom, M. (2018, Jul). Mars Aerosol Tracker (MAT): An Areostationary SmallSat to Monitor Dust Storms and Water Ice Clouds. In *42nd cospar scientific assembly* (Vol. 42, p. B0.2-16-18).

Montabone, L., Lewis, S. R., & Read, P. L. (2005). Interannual variability of Martian dust storms in assimilation of several years of Mars global surveyor observations. *Advances in Space Research*, *36*, 2146-2155. doi: 10.1016/j.asr.2005.07.047

Mulholland, D. P., Read, P. L., & Lewis, S. R. (2013). Simulating the interannual variability of major dust storms on Mars using variable lifting thresholds. *Icarus*, *223*, 344-358. doi: 10.1016/j.icarus.2012.12.003

Navarro, T., Madeleine, J.-B., Forget, F., Spiga, A., Millour, E., Montmessin, F., & Määttänen, A. (2014). Global Climate Modeling of the Martian water cycle with improved microphysics and radiatively active water ice clouds. *Journal of Geophysical Research (Planets)*. doi: 10.1002/2013JE004550

Newman, C. E., & Richardson, M. I. (2015). The impact of surface dust source exhaustion on the martian dust cycle, dust storms and interannual variability, as simulated by the MarsWRF General Circulation Model. *Icarus*, *257*, 47-87. doi: 10.1016/j.icarus.2015.03.030

Ryan, J. A., & Henry, R. M. (1979). Mars atmospheric phenomena during major dust storms as measured at surface. *J. Geophys. Res.*, *84*, 2821-2829.

Shirley, J., Kleinböhl, A., Kass, D., Steele, L., Heavens, N., Suzuki, S., … McCleese, D. (2019). Rapid expansion and evolution of a regional dust storm in the acidalia corridor during the initial growth phase of the martian global dust storm of 2018. *Geophysical Research Letters*, *0*(ja). doi: 10.1029/2019GL084317

Smith, M. D. (2019). Themis observations of the 2018 mars global dust storm. *Journal of Geophysical Research - Planets*, accepted.

Spiga, A., Banfield, D., Teanby, N. A., Forget, F., Lucas, A., Kenda, B., … Banerdt, W. B. (2018). Atmospheric Science with InSight. *Space Science Reviews*, *214*, 109. doi: 10.1007/s11214-018-0543-0

Spiga, A., Faure, J., Madeleine, J.-B., Määttänen, A., & Forget, F. (2013, April). Rocket dust storms and detached dust layers in the Martian atmosphere. *Journal of Geophysical Research (Planets)*, *118*, 746-767. doi: 10.1002/jgre.20046

Spiga, A., Hinson, D., Madeleine, J., Navarro, T., Millour, E., Forget, F., & Montmessin, F. (2017). Snow precipitation on Mars driven by cloud-induced nighttime convection. *Nature Geoscience*, *10*, 652-657. doi: 10.1038/ngeo3008

Streeter, P. M., Lewis, S. R., Patell, M. R., Holmes, J. A., & Kass, D. M. (2019). Surface warming during the 2018/Mars Year 34 Global Dust Storm. *Geophysical Research Letters*, *0*(ja). doi: 10.1029/2019GL083936

Szwast, M. A., Richardson, M. I., & Vasavada, A. R. (2006). Surface dust redistribution on Mars as observed by the Mars Global Surveyor and Viking orbiters. *Journal of Geophysical Research (Planets)*, *111*(E10), 11008. doi: 10.1029/2005JE002485

Sánchez-Lavega, A., del Río-Gaztelurrutia, T., Hernández-Bernal, J., & Delcroix, M. (2019). The onset and growth of the 2018 martian global dust storm. *Geophysical Research Letters*, *46*(11), 6101-6108. doi: 10.1029/2019GL083207

Vincendon, M., Audouard, J., Altieri, F., & Ody, A. (2015). Mars Express measurements of surface albedo changes over 2004-2010. *Icarus*, *251*, 145-163. doi: 10.1016/j.icarus.2014.10.029

Viúdez-Moreiras, D., Newman, C. E., de la Torre, M., Martínez, G., Guzewich, S., Lemmon, M., ... Gómez-Elvira, J. (2019). Effects of the my34/2018 global dust storm as measured by msl rems in gale crater. *Journal of Geophysical Research: Planets*, *124*(7), 1899-1912. Retrieved from `https://agupubs.onlinelibrary.wiley.com/doi/abs/10.1029/2019JE005985` doi: 10.1029/2019JE005985

Wang, C., Forget, F., Bertrand, T., Spiga, A., Millour, E., & Navarro, T. (2018). Parameterization of Rocket Dust Storms on Mars in the LMD Martian GCM: Modeling Details and Validation. *Journal of Geophysical Research (Planets)*, *123*, 982-1000. doi: 10.1002/2017JE005255

Wilson, R. W., & Hamilton, K. (1996). Comprehensive model simulation of thermal tides in the Martian atmosphere. *J. Atmos. Sci.*, *53*, 1290-1326.

Withers, P. (2012, Sep). Empirical Estimates of Martian Surface Pressure in Support of the Landing of Mars Science Laboratory. *Space Science Reviews*, *170*(1-4), 837-860. doi: 10.1007/s11214-012-9876-2

Xiaohua, F., Ma, Y., Lee, Y., Bougher, S., Liu, G., Benna, M., ... Jakosky, B. (2019). Mars dust storm effects in the ionosphere and magnetosphere and implications for atmospheric carbon loss. *Journal of Geophysical Research - Space Physics*, accepted.

Zurek, R. W. (1982). Martian great dust storm, an update. *Icarus*, *50*, 288-310.

Zurek, R. W., & Martin, L. J. (1993). Interannual variability of planet-encircling dust storms on Mars. *J. Geophys. Res.*, *98*(E2), 3247-3259.